This article has been accepted for inclusion in a future issue of this journal. Content is final as presented, with the exception of pagination.

Mapping Forest and Their Spatial–Temporal Changes From 2007 to 2015 in Tropical Hainan Island by Integrating ALOS/ALOS-2 L-Band SAR and Landsat Optical Images

Bangqian Chen, Xiangming Xiao, Huichun Ye, Jun Ma, Russell Doughty, Xiangping Li, Bin Zhao, Zhixiang Wu, Rui Sun, Jinwei Dong, Yuanwei Qin, and Guishui Xie

***Abstract*—Accurately monitoring forest dynamics in the tropical regions is essential for ecological studies and forest management. In this study, images from phase-array L-band synthetic aperture radar (PALSAR), PALSAR-2, and Landsat in 2006–2010 and 2015 were combined to identify tropical forest dynamics on Hainan Island, China. Annual forest maps were first mapped from PALSAR and PALSAR-2 images using structural metrics. Those pixels with a high biomass of sugarcane or banana, which are widely distributed in the tropics and subtropics and have similar structural metrics as forests, were excluded from the SAR-based forest maps by using phenological metrics from time series Landsat imagery. The optical–SAR-based forest maps in 2010 and 2015 had high overall accuracies (OA) of 92–97% when validated with ground reference data. The resultant forest map in 2010 shows good spatial agreement with public optical-based forest maps (OA = 88–90%), and the annual forest maps (2007–2010) were spatiotemporally consistent and more accurate than the PALSAR-based forest map from the Japan Aerospace Exploration Agency (OA = 82% in 2010). The areas of forest gain, loss, and net change on Hainan Island from 2007 to 2015 were 415 000 ha (+2.17% yr^{-1}), 179 000 ha (–0.94% yr^{-1}), and 236 000 ha (+1.23% yr^{-1}), respectively. About 95% of forest gain and loss occurred in those areas with an elevation less than 400 m, where deciduous rubber, eucalyptus plantations, and urbanization expanded rapidly. This study demonstrates the potential of PALSAR/PALSAR-2/Landsat image fusion for monitoring annual forest dynamics in the tropical regions.**

***Index Terms*—Forest loss and gain, high biomass crops, image data fusion, land surface water index (LSWI), normalized difference vegetation index (NDVI).**

Manuscript received June 6, 2017; revised November 30, 2017 and January 9, 2018; accepted January 9, 2018. This work was supported in part by the Hainan Provincial Department of Science and Technology under Grant ZDKJ2016021, in part by the National Natural Science Foundation of China under Grant 41571408 and Grant 41701510, in part by the Earmarked Fund for China Agriculture Research System under Grant CARS-34-GW5, in part by the Fundamental Research Funds of Rubber Research Institute, Chinese Academy of Tropical Agricultural Sciences under Grant 1630022017016 and Grant 1630022015012, and in part by the U.S. NASA Land Use and Land Cover Change program under Grant NNX14AD78G. *(Corresponding author: Xiangming xiao.)*

B. Chen is with the Danzhou Investigation and Experiment Station of Tropical Crops, Ministry of Agriculture, Rubber Research Institute, Chinese Academy of Tropical Agricultural Sciences, Danzhou 571737, China, and also with the Ministry of Education Key Laboratory for Biodiversity Science and Ecological Engineering Institute of Biodiversity Sciences, Fudan University, Shanghai 200438, China (e-mail: chbq40@163.com).

X. Xiao is with the Ministry of Education Key Laboratory for Biodiversity Science and Ecological Engineering, Institute of Biodiversity Sciences, Fudan University, Shanghai 200438, China, and also with the Department of Microbiology and Plant Biology, and the Center for Spatial Analysis, University of Oklahoma, Norman, OK 73019 USA (e-mail: xiangming.xiao@ou.edu).

H. Ye is with the Key Laboratory of Digital Earth Science, Institute of Remote Sensing and Digital Earth, Chinese Academy of Sciences, Beijing 100094, China, and also with the Hainan Key Laboratory of Earth Observation, Sanya 572029, China (e-mail: yehuichun000@126.com).

J. Ma, X. Li, and B. Zhao are with the Ministry of Education Key Laboratory for Biodiversity Science and Ecological Engineering, Institute of Biodiversity Sciences, Fudan University, Shanghai 200438 China (e-mail: mmjun526@163.com; xiangpingli@fudan.edu.cn; zhaobin@fudan.edu.cn).

R. Doughty, J. Dong, and Y. Qin are with the Department of Microbiology and Plant Biology, and the Center for Spatial Analysis, University of Oklahoma, Norman, OK 73019 USA (e-mail: russell.doughty@ou.edu; jinwei.dong@ou.edu; yuanwei.qin@ou.edu).

Z. Wu, R. Sun, and G. Xie are with the Danzhou Investigation and Experiment Station of Tropical Crops, Ministry of Agriculture, Rubber Research Institute, Chinese Academy of Tropical Agricultural Sciences, Danzhou 571737, China (e-mail: wzxrri@163.com; sunrui_85@163.com; Xie23300459@163.com).

Color versions of one or more of the figures in this paper are available online at http://ieeexplore.ieee.org.

Digital Object Identifier 10.1109/JSTARS.2018.2795595

I. Introduction

TROPICAL forests exert a profound influence on climate, biodiversity, and ecosystem services [1]. Rapid deforestation and degradation of tropical forests, which lost approximately 13 million ha per year in the period 2000–2010 and constituted about 15% of the world's anthropogenic greenhouse gas emissions, has been underway in the tropics since the 1980s [2]–[4]. Both local decision makers and international initiatives such as reducing emissions from deforestation and forest degradation in developing countries are calling for accurate, annual maps of tropical forests at fine spatial resolution, which can be used to better assess biological conservation, carbon and water cycles, and to develop improved plans for sustainable management [3]–[8].

Remote sensing is an essential tool for assessing forest cover dynamics from the local to global scale. Numerous studies have used optical images to generate forest cover maps, including moderate resolution images such as Landsat thematic mapper (TM) and enhanced thematic mapper plus (ETM+) [9]–[12], coarse resolution images such as moderate resolution imaging spectroradiometer (MODIS) [13], [14] and NOAA advanced very high resolution radiometer [15], and combined imagery using multiple sensors [12], [16]–[18]. Coarse resolution images have the potential to track the annual dynamic of large, intact forests, but are not suitable for the identification of small and fragmented forests. Very high-resolution images such as worldview [19] can provide more details about forests, but these images have not been used to monitor annual dynamics over large areas due to high monetary and computational costs. Recently, several 30 m scale global forest maps have been generated, such as fine resolution observation and monitoring-global land cover (FROM-GLC) by Tsinghua University [20], global forest change (GFC) [9] by the University of Maryland, and GlobeLand30 by the National Geomatics Center of China [10]. These publicly available maps were generated from analyses of Landsat data [9], [20] or the combination of Landsat and the Chinese environmental protection and disaster monitoring satellite (HJ-1) [10]. Only GFC provides annual maps of forest loss, and none of these Landsat-based datasets provide annual dynamics of gain and net change because good quality images are lacking due to persistent cloud cover [21]. In addition, landscapes in tropical zones are typically fragmented into small patches of land use and land cover types, making land cover classification more complicated [22], [23].

The synthetic aperture radar (SAR) acquired images not affected by cloud cover. Long wavelength SARs, such as P- and L-bands, easily penetrate the forest canopy and capture information on the forest structure, and are therefore useful in forest mapping [3], [24]. With the public availability of 50 and 25 m phased array type L-band synthetic aperture radar (PALSAR) and PALSAR-2 orthorectified mosaic images produced by the Japan Aerospace Exploration Agency (JAXA), the application of SAR-based data to forest mapping has greatly accelerated from local to global scales [6], [24], [25]. Recently, annual, global-scale forest/nonforest (F/NF) maps (25 m) from 2007 to 2010 were released using variable HV thresholds based on the 25 m PALSAR mosaic data [25]. However, forest maps derived from SAR images solely may have some shortcomings, because SAR backscatter energy, which relies on the physical structure, may be affected by moisture content and underlying soil conditions [26], [27]. Buildings in urban or rural areas (built-up) and high biomass croplands (e.g., sugarcane and banana plantations) may also have backscatter coefficients like that of forests, which may, therefore, reduce the accuracy of PALSAR-based forest maps. These land cover types need to be identified and eliminated in advance or during postclassification [25], [28], [29].

Recently, several studies reported forest cover mapping through integration of both optical and L-band SAR images [30]–[32], particularly Landsat and PALSAR data [3], [33]–[35]. Most of them generated forest cover maps at a specific time point or over a multiyear interval (e.g., five years). The increasing availability of time series optical and SAR data for large areas, batch preprocessing software/tools for cloud detection (e.g., Fmask [21]) and atmospheric correction (e.g., Landsat ecosystem disturbance adaptive processing system, LEDAPS [36]), and cloud-based computation resources (e.g., Google Earth Engine, GEE, https://earthengine.google.com) enables a shift from traditional bitemporal change detection analyses to time series based change detection analyses [3]. The latter approach could provide more details about forest location, land cover change, and spatial scale over time through complementary structural, spectral, and phenological metrics from SAR and time series optical data.

In our previous study, we developed a decision tree based forest mapping algorithm using 25 m PALSAR and time series Landsat TM/ETM+ data [35], [37]. We first identified and generated forest maps using PALSAR data, then improved map accuracy by eliminating misclassified pixels associated with built-up areas using the maximum normalized difference vegetation index (NDVI) derived from time series Landsat data. However, commission error from high biomass crops such as sugarcane and banana, which are widely distributed in tropics and subtropics, still needs to be addressed when this algorithm is applied to quantify forested areas in a year or multiple years over the complex and fragmented tropical landscapes [22], [23]. In addition, the availability of global mosaic data obtained using the PALSAR-2 sensor onboard advanced land observation satellite-2 (ALOS-2) makes it possible to quantify and monitor tropical forest dynamics over many years (2007–2010, 2015 to present). The utility of our pixel- and phenology-based algorithm with PALSAR-2 and Landsat ETM+ and operational land imager (OLI) needs to be evaluated, too.

The objectives of this study are to

1) analyze whether our mapping algorithm developed for ALOS PALSAR and Landsat TM/ETM+ could be applied to ALOS-2 PALSAR-2 and Landsat ETM+/OLI images;
2) develop a feasible algorithm to eliminate commission errors from misclassification of high biomass crops like sugarcane and banana; and
3) conduct novel forest mapping and change detection in the second decade of the 21st century.

II. Materials and Methods

A. Study Area

The study area is Hainan Island [19°20′N–20°10′N, 108°21′E–111°03′E, about 3.38 million ha, Fig. 1(a)], China. The topography of the island is characterized by hills in the central regions and lowlands along the coasts. Wuzhi Mountain, with an elevation of 1867 m above sea level, is the highest mountain on the island. The climate varies from tropical to subtropical. The annual mean temperature is approximately 23–25 °C, and monthly temperature varies between ~16 °C in January and ~30 °C from May to July. The average annual precipitation is 1500–2000 mm, 80% of which occurs during the rainy season from May to October. The spatial distribution of precipitation, however, can be as high as 2400 mm in the central and eastern area, and as low as 900 mm in the coastal areas of the southwest. Historically, natural forests almost completely covered the island. However, since the 1950s, more than half of the natural forests have been converted to industrial forests, such as natural rubber (*Hevea brasiliensis*) or eucalyptus (*Eucalyptus robusta*), and other land-use types to meet economic demands. In the 1980s, the coverage of natural forests dropped to 9.7%, down from 25.7% in 1956 [38]. After the 1980s, extensive reforestation and afforestation occurred on the island. Forest coverage reached 61.5% with an area of 2.11 million ha in 2014 [39].

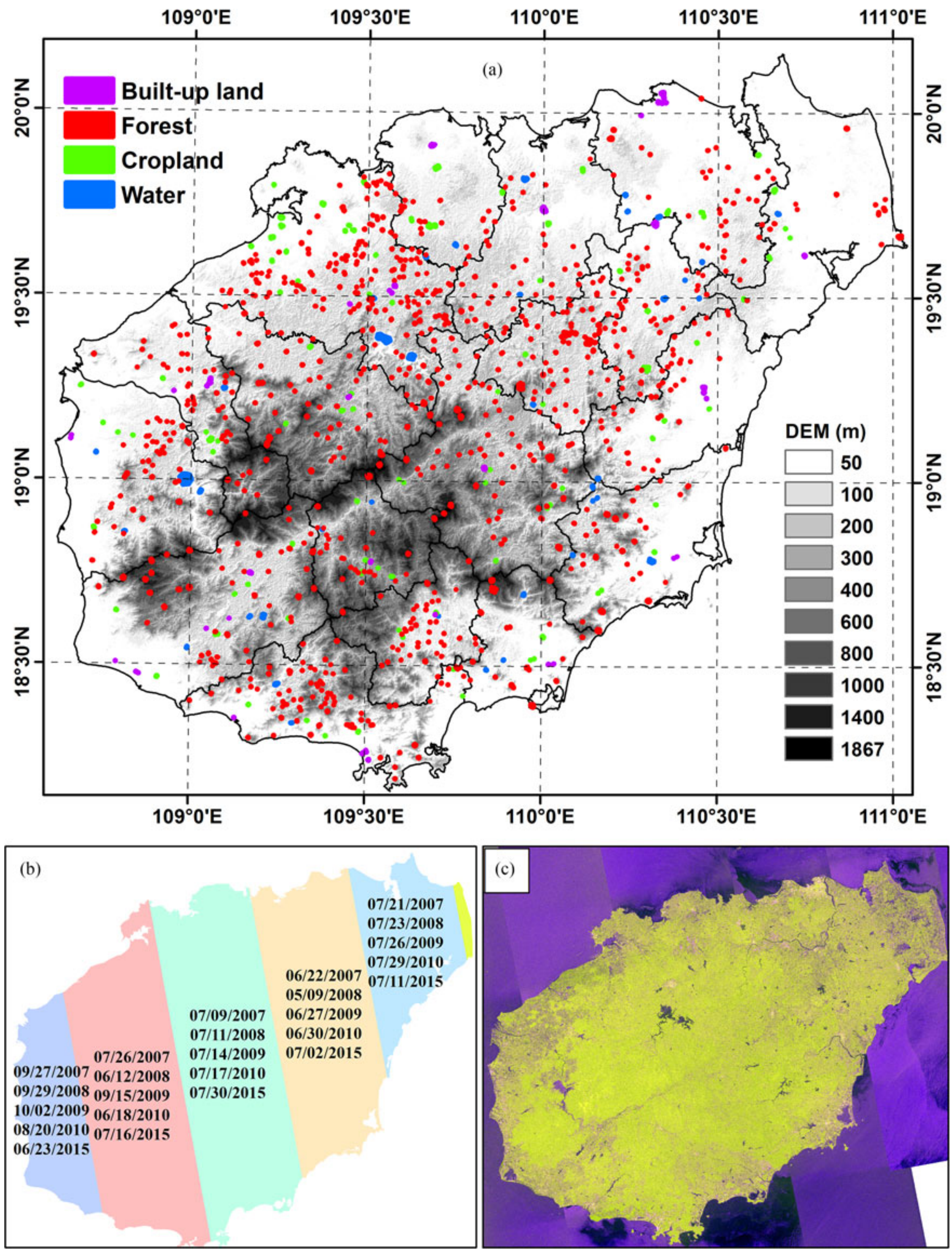

Fig. 1. Study area and ALOS/ALOS-2 L-band SAR images: (a) topography of Hainan Island with county boundaries and the locations of ground reference sites (GRS) of 2015 used for algorithm training and accuracy assessment (corresponding statistical data are presented in Tables I and S1), (b) acquisition dates of the PALSAR/PALSAR-2 imagery, and (c) false color composite of 25 m PALSAR-2 orthorectified mosaic imagery (R/G/B = HH/HV/HH – HV) of Hainan Island in 2015.

B. Ground Reference Data

Same ground reference sites (GRS) as reported in our previous study [35] to map forest for 2010 were used here. These GRS were determined to be areas of forest, built-up, water, and cropland using ground-based and geotagged landscape photos and Google Earth's (GE) very high spatial resolution (VHSR) satellite images acquired circa 2010 [35]. The landscape photos were uploaded to the Global Geo-Referenced Field Photo Library (http://www.eomf.ou.edu/photos/), a free and public portal for people to download, upload, and share GPS-embedded land

TABLE I
STATISTICAL INFORMATION OF GRS USED IN THIS STUDY

		Forest	Built-up	Water	Cropland
Y2010	Training	275 (1599)	13 (241)	13 (1091)	32 (421)
	Validation	649 (3065)	30 (419)	29 (1047)	77 (505)
Y2015	Training	333 (1591)	13 (365)	16 (1418)	22 (167)
	Validation	776 (4070)	30 (278)	36 (658)	52 (734)

The first values at each cell are the number of GRS, and the second values in parentheses are total area of the GRS in hectares. Built-up, water, and croplands were regarded as nonforest. To evaluate the 2015 F/NF map, 677 F/NF GRS at 0.25 ha (50×50 m^2) were randomly generated by a computer.

cover photos (see Fig. S1). During GRS delineation, rainforest, plantations of rubber and eucalyptus were regarded as forest, while buildings and impervious surfaces, like roads, were treated as built-up. Cropland included paddy rice, dry land, and other crops.

The 2010 GRS was updated and few more were added with references of geotagged landscape photos taken in February 2015 and October 2016, and GE VHSR images acquired circa 2015. These updated 2015 GRS [see Fig. 1(a)] were used for developing and validating our forest mapping algorithm using PALSAR-2 and Landsat ETM+/OLI imagery. The statistical information of GRS of 2010 and 2015 is presented in Table S1. Both the GRS of 2010 and 2015 were randomly divided into training (30%) and validation (70%) datasets, using NOAA/NOS/NCCOS/CCMA Biogeography Branch's Design Tool for ArcGIS (see Table I).

Furthermore, random GRS with areas of 0.25 ha (50×50 m^2) was generated using GEE's random function for map accuracy assessment. The island is about $2° \times 2°$ in size, so 800 random GRS (about 200 per $1° \times 1°$ grid) was created within a 5-km buffer zone of the entire island (see Fig. S2). These GRS were identified as forest (forest coverage $> 90\%$) or nonforest (forest coverage $< 10\%$) with GE VHSR satellite images acquired circa 2015. In total, we had 351 forests, 326 nonforest, and 123 mixed forest GRS. These 677 F/NF GRS were used to evaluate the accuracy of the 2015 forest map. To avoid confusion, we called these GRS as random GRS, while the empirical delineated ones as empirical GRS.

C. Satellite Image Data and Preprocessing

1) PALSAR and PALSAR-2 Data and Preprocessing: The annual 25 m PALSAR orthorectified mosaic data from 2007 to 2010 and PALSAR-2 mosaic data in 2015 were downloaded from the ALOS Research and Application Project overseen by JAXA's Earth Observation Research Center (http://www.eorc.jaxa.jp/). Both PALSAR and PALSAR-2 are L-band SARs that can transmit and receive horizontally or vertically polarized signals, allowing for horizontal transmission and reception (HH) and horizontal transmission and vertical reception (HV). Six strip images covered the island, and most images were acquired in June and July [see Fig. 1(b)]. These datasets were already topographically (slope) corrected, radiometrically calibrated, and geo-referenced to geographical coordinates [25]. The HH and HV bands were converted from amplitudes into normalized radar cross-section backscatter (dB), using [40]

$$\gamma^0(\mathrm{dB}) = 10\log_{10} DN^2 + CF \tag{1}$$

where γ^0 is the backscattering coefficient, DN is the digital number value in HH or HV, and CF is the absolute calibration factor set at –83. Two composite images of ratio (HH/HV) and difference (HH – HV) were generated for classification [30]. The calculation of backscatter coefficients and generation of ratio and difference bands were finished in ENVI/IDL (http://www.harrisgeospatial.com/). As shown in Fig. 1(c), forests are shown in a light green color in the false color composite of PALSAR-2 imagery in 2015. PALSAR and PALSAR-2 images were not available in GEE's public data catalog, so they were manually uploaded as GEE assets for analysis.

2) Landsat Data and Preprocessing: Hainan Island is covered by four path/rows Landsat images [Worldwide Reference System (WRS-2) 123/046, 123/047, 124/046 and 124/047]. A total of 643 standard level-one terrain-corrected (L1T) TM/ETM+/OLI surface reflectance (SR) images, from 2006 to 2010 and 2014 to 2015, were used (see Fig. 2) and were available in GEE as image collections. The TM/ETM+ SR data were processed using LEDAPS [36], while Landsat OLI SR data were generated by LaSRC software [41]. Poor quality observations caused by clouds and shadows were identified by Cfmask [21]. Pixels that are cloud-free and not in ETM+ scan-line-off strips were selected as good quality observations. The annual total number of observations was the lowest in 2008, and the highest in 2015, and most of the study area has more than 20 good-quality observations throughout the five years. For each Landsat TM/ETM+/OLI imagery, NDVI [42], enhanced vegetation index (EVI) [43], and land surface water index (LSWI) [44], [45] were calculated using

$$\mathrm{NDVI} = \frac{\rho_{\mathrm{NIR}} - \rho_{\mathrm{red}}}{\rho_{\mathrm{NIR}} + \rho_{\mathrm{red}}} \tag{2}$$

$$\mathrm{EVI} = 2.5 \times \frac{\rho_{\mathrm{NIR}} - \rho_{\mathrm{red}}}{\rho_{\mathrm{NIR}} + 6 \times \rho_{\mathrm{red}} - 7.5 \times \rho_{\mathrm{blue}} + 1} \tag{3}$$

$$\mathrm{LSWI} = \frac{\rho_{\mathrm{NIR}} - \rho_{\mathrm{SWIR}}}{\rho_{\mathrm{NIR}} + \rho_{\mathrm{SWIR}}} \tag{4}$$

where ρ_{blue}, ρ_{red}, ρ_{NIR}, and ρ_{SWIR} are the blue (450–520 nm), red (630–690 nm), near-infrared (NIR, 760–900 nm), and shortwave-infrared (SWIR, 1550–1750 nm) SR bands of Landsat TM/ETM+/OLI imagery, respectively. Annual maximum NDVI maps (NDVI$_{\max}$, hereinafter) and frequency maps, based on the criteria of NDVI < 0.5 and LSWI < 0.1 (see Section II-D), were generated using Landsat imagery acquired in the previous and current years (e.g., 2006 and 2007 for 2007) for 2007, 2008, 2009, and 2010, and 2015, respectively.

3) Data Fusion of PALSAR/PALSAR-2 and Landsat Data: The 25 m PALSAR and PALSAR-2 data were resampled to 30 m to match the spatial resolution of Landsat images using a nearest neighbor sampling method, which does not introduce new pixel DN vectors into image statistical distribution and is good for classification by statistical techniques [46]. Then, a data cube was built for PALSAR, PALSAR-2, and Landsat (PALSAR/Landsat, hereafter) images at 30 m spatial resolution. The resultant PALSAR/Landsat data cube was used to generate annual forest maps on the island.

This article has been accepted for inclusion in a future issue of this journal. Content is final as presented, with the exception of pagination.

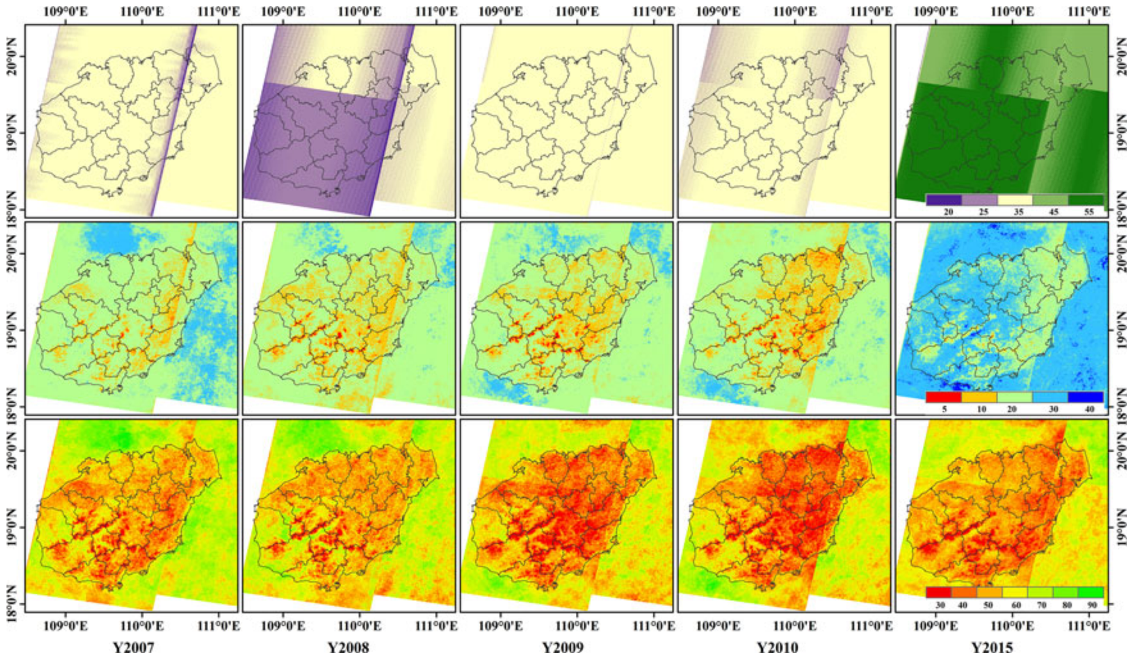

Fig. 2. Data availability of annual Landsat TM/ETM+/OLI collection of Hainan Island from 2007 to 2015. Images in first rows are number of total observation, in second row are number of good observation, and in third row are percentage of good observation from 2007 to 2015.

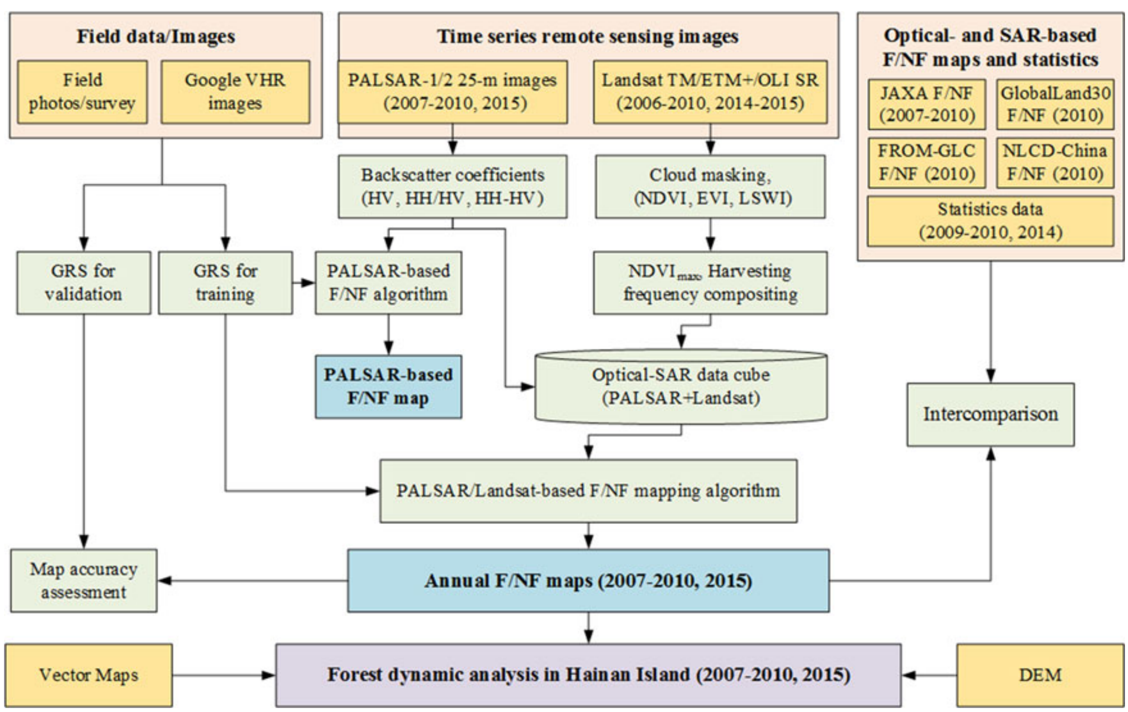

Fig. 3. Workflow for mapping tropical forest through analysis of ALOS PALSAR/PALSAR-2 and time series Landsat TM/ETM+/OLI imagery.

D. Algorithms for Forest Mapping

According to FAO, forest is defined as land spanning more than 0.5 ha with tree height of >5 m and canopy cover of >10% [47]. This forest definition includes both forest structure and canopy information, which can be quantified by a PALSAR/Landsat data cube. Our forest mapping workflow is presented in Fig. 3. Forest was first identified using structure-based metrics from PALSAR/PALSAR-2 images, then reduced commission errors using forest canopy metrics from time series Landsat data. A structure-based signature analysis of forest/nonforest (F/NF) (see Fig. S3) was performed with PALSAR data in 2010, and a rule-based forest classification algorithm ($-17 < \mathrm{HV} < -9$ and $0.35 < \mathrm{Ratio} < 0.85$ and $1.5 < \mathrm{Diff} < 9.0$, Fig. S4, rounded 5% and 95% bounds were used as thresholds) was developed [35]. Similar signature anal-

This article has been accepted for inclusion in a future issue of this journal. Content is final as presented, with the exception of pagination.

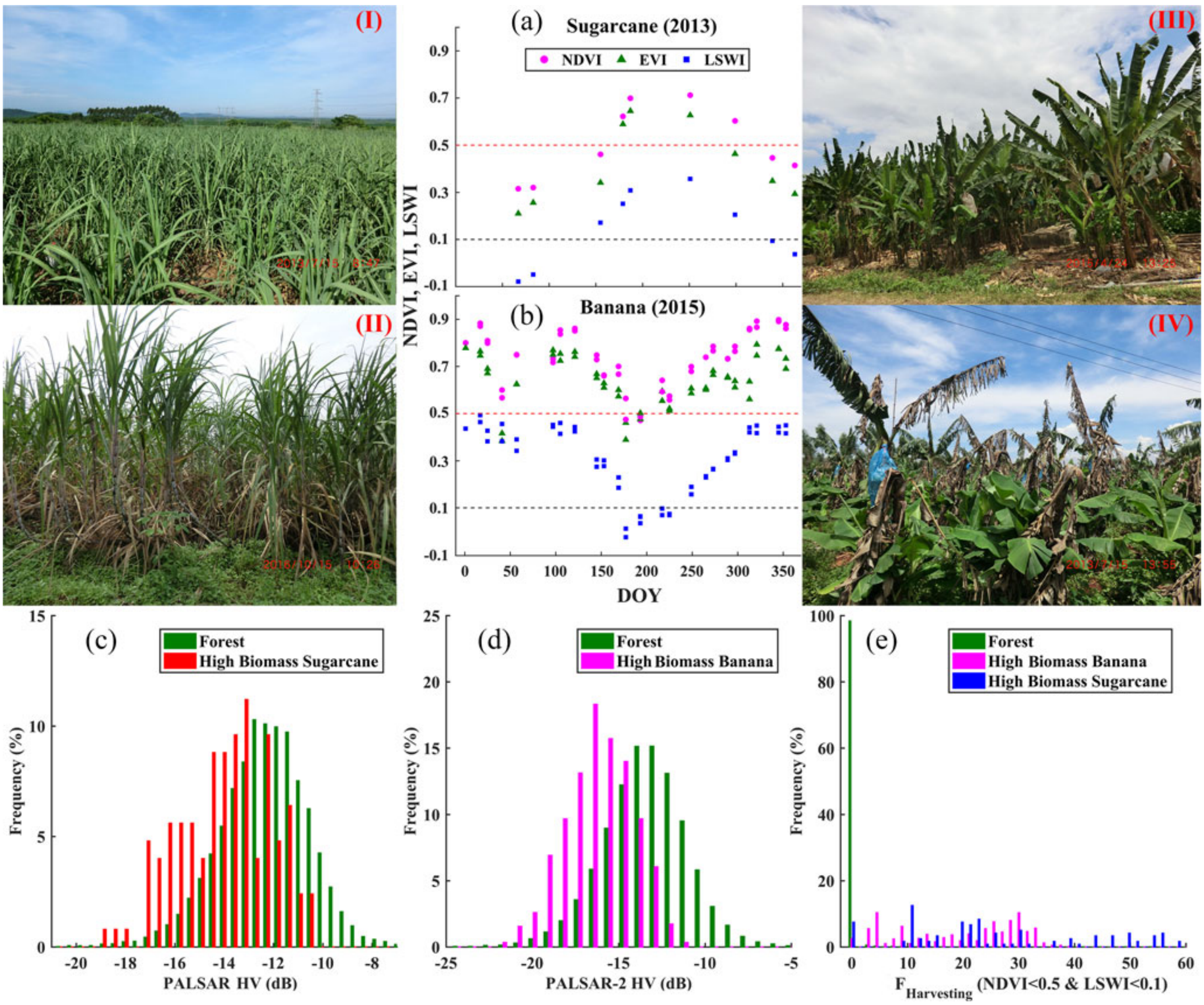

Fig. 4. Signature analyses of forests, high biomass sugarcane, and banana plantations: GRS Photos of (I) low biomass sugarcane plantation taken on 2013/07/15 (19.5871 °N, 109.3468 °E), (II) high biomass sugarcane taken on 2016/10/15 (19.6043 °N, 109.3468 °E), (III) high biomass banana plantation taken on 2015/04/24 (19.3856 °N, 109.2839 °E), and (IV) harvest banana plantation taken on 2013/07/15 (19.8085 °E, 109.8357 °E). Temporal profile of Landsat NDVI/LSWI/EVI for (a) sugarcane plantation from GRS I and (b) banana plantation from GRS III. Histograms of (c) forest and high biomass sugarcane plantation in PALSAR HV band, (d) forest and high biomass banana plantation in PALSAR-2 HV band, and (e) F_{Harvest} (NDVI $<$ 0.5 and LSWI $<$ 0.1) of forest, high biomass banana, and sugarcane.

ysis of F/NF based on 2015 training GRS was performed on PALSAR-2 (see Fig. S5) data. The F/NF histograms on PALSAR-2 HH, HV, ratio, and difference bands had similar patterns with results based on PALSAR, but differ slightly in boundary values. Therefore, a similar forest classification algorithm for PALSAR-2 imagery was built using rounded 5% and 95% confidence intervals of the histograms, specifically, $-19 < \text{HV} < -7.5, 0.20 < \text{Ratio} < 0.95$, and $0 < \text{Diff} < 9.5$. In addition, the temporal variability of forest backscatter coefficients during 2007–2009 was evaluated using the training GRS of 2010 (see Fig. S6). The results indicated that the backscatter coefficients of forest in HH, HV, ratio, and difference during 2007–2010 were quite stable. Therefore, annual forest maps during 2007–2009 were generated using the same algorithm developed using PALSAR imagery from 2010 (see Fig. S4). For spatial consistency, a 5 $\times$ 5 median filter was performed to reduce the salt-and-pepper noise on the SAR-based F/NF maps.

Our previous study reported canopy-based signature analyses with time series Landsat images in 2010 using yearly maximum NDVI values greater than 0.65 ($\text{NDVI}_{\max} > 0.65$, Fig. S7) as a threshold for forest canopy. Those pixels with $\text{NDVI}_{\max}$ less than 0.65 were assumed as nonforest canopy, including the built-up land cover, such as urban areas [35]. In this study, we found high biomass crops such as sugarcane and banana plantations, which are widely distributed in tropical and subtropics, have similar HV backscatter coefficients as forests in both PALSAR and PALSAR-2 [see Fig. 4(c) and (d)] data. Those croplands would be misclassified as forest if the SAR data were acquired in a season when those croplands have high biomass. By observing the phenological change of sugarcane and banana plantations [see Fig. 4(a) and (b)], we found that they usually have low values of NDVI (< 0.5) and LSWI (< 0.1) after harvest due to the exposure of crop residuals and soils [48]. The variation in crop phenology and climate could bias the harvest signal from a time-specific image or a single imagery composite. Therefore, a frequency-based harvest signal (NDVI < 0.5 and LSWI < 0.1) from analyses of all Landsat TM/ETM+/OLI images in April to December was used here. Images in January–March were not used as rubber tree leaves senesce in subtropical and northern tropical zones during this period [35]. The harvest frequency map was generated in two steps. First, harvest was determined using

$$\text{Harvest} = \begin{cases} 1 & \text{LSWI} < 0.1 \text{ and NDVI} < 0.5 \\ 0 & \text{Other values} \end{cases}. \quad (5)$$

Second, calculating harvest frequency using

$$F_{\text{Harvest}} = \frac{\sum N_{\text{Harvest}}}{\sum N_{\text{Total}} - \sum N_{\text{Bad}}} \times 100 \quad (6)$$

where F_{Harvest} is the harvest frequency scaled to 0 and 100, N_{Harvest} is the number of images where LSWI < 0.1 and NDVI < 0.5, N_{Total} is the number of total observations, and N_{Bad} is the number of bad observations (e.g., clouds, shadows, and ETM+ scan-line-off strips). A harvest frequency of 5% was selected as a threshold for nonforest pixels that could be associated with high biomass croplands such as sugarcane and banana plantations [see Fig. 4(e)].

Based upon these analyses, we proposed a PALSAR/Landsat-based forest mapping algorithm using the following criteria: 1) forest signatures in PALSAR or PALSAR-2; 2) $\text{NDVI}_{\max} > 0.65$; and 3) $F_{\text{Harvest}} < 5\%$ (Apr.–Dec.).

E. Regional Implementation of the PALSAR/Landsat-Based Forest Mapping Algorithm

The algorithm was running for individual pixels and generated annual forest maps for 2007–2010 and 2015 using the PALSAR/Landsat data cube. For temporal consistency over the years at individual pixels, two postclassification consistency analyses were carried out on the PALSAR/Landsat-based F/NF maps.

First, the consistency in HV values was evaluated. A previous study found that the average ${\gamma^0}_{\text{HV}}$ of the deforested area was systematically lower by 1–4 dB than that of natural forest, and thus, a threshold of 1 dB from time series difference of PALSAR ${\gamma^0}_{\text{HV}}$ was used to detect tropical deforestation in Indonesia from 2007 to 2010 [6]. Based on this observation, a 1 dB difference in the HV band was used to check for consistency in the annual F/NF maps. The PALSAR HV image in 2007 was taken as a benchmark and generated difference images of $\text{HV}_{2008\text{-}2007}$, $\text{HV}_{2009\text{-}2008}$, $\text{HV}_{2010\text{-}2009}$, and $\text{HV}_{2015\text{-}2010}$ for consistency analysis. Using 2007–2008 as an example, forest gain should meet $\text{HV}_{2008\text{-}2007} > 1$ dB while forest loss should satisfy $\text{HV}_{2008\text{-}2007} < -1$ dB. The forest gain and loss are more evident in $\text{HV}_{2015\text{-}2010}$ from PALSAR-2 and PALSAR (see Fig. S8); therefore, the thresholds of 1/–1 dB are still suitable for forest gain/loss consistent analysis between PALSAR and PALSAR-2. Second, a logical consistency check was performed on the four-consecutive annual F/NF maps with a focus on 2008–2009 (2 years) out of 2007–2010 (4 years) [37]. A total of 16 different change combinations, from N → N → N → N to F → F → F → F (N indicates nonforest, F represents forest), were analyzed. Unreasonable changes of N → N → F → N and N → F → N → N, as well as F → F → N → F and F → N → F → F, were regarded as classification errors or image noise and were converted to N → N → N → N and F → F → F → F, respectively. The other unreasonable changes of N → F → N → F, N → F → F → N, F → N → N → F, and F → N → F → N were unprocessed because of too many uncertainties.

F. Map Accuracy Assessment for PALSAR/Landsat-Based Forest Maps

The resultant 2010 F/NF map was evaluated using empirical GRS of 2010. The resultant 2015 F/NF map was evaluated using 70% of empirical and random GRS. The error-adjusted matrix in terms of proportion of area and estimates of producer's accuracy (PA), user's accuracy (UA), and overall accuracy (OA) with 95% confidence intervals was used to evaluate map accuracy as proposed by a previous study [49]. The error-adjusted matrix was a statistically robust and transparent approach for assessing accuracy, a method that has recently become increasingly common [49]–[51]. The annual F/NF maps of 2007, 2008, and 2009 were generated using the same algorithm with PALSAR/Landsat data. These F/NF maps were not validated with independent GRS by considering the signal of PALSAR (see Fig. S6) and Landsat data were stable during these periods.

G. Intercomparison With Other Available Forest Maps

The empirical GRS of 2010 were also used to assess the public F/NF maps of 2010 from 1) JAXA, which produced the map using 25 m PALSAR data [25], and optical-based data of 2) FROM-GLC (segmentation approach version) [20] and 3) GlobeLand30 [10]. Since annual F/NF maps of 2007–2010 cannot be generated from GFC percentage tree cover in 2000 and annual GFC loss maps [9], GFC maps were not incorporated for comparison.

Subsequently, maps of forest cover percentage at 1-km resolution were generated from the 30 m spatial resolution F/NF maps of PALSAR/Landsat, FROM-GLC, and GlobeLand30 to match the spatial resolution of the National Land Cover Dataset of China (NLCD) F/NF map. The spatial distribution of forests in these F/NF maps was compared at the county level.

H. Forest Cover Dynamic Analysis Over Years

Forest cover was divided into 10 groups according to elevation ranges of 0–50, 50–100, 100–200, 200–300, 300–400, 400–600, 600–800, 800–1000, 1000–1400, and 1400–1867 m. Annual forest area for each elevation group was calculated and their dynamics were explored. In addition, spatial–temporal consistency of the F/NF maps was evaluated pixel-by-pixel by counting the occurrences of forest during 2007–2015 (e.g., 1, 2, 3 . . . times), and forest area was calculated according to the frequency of forest occurrence. Maps of consistent forest, forest gain, forest loss, and consistent nonforest during 2007 and 2015 were produced, and the area of forest gain and loss at different elevation

TABLE II
ACCURACY ASSESSMENT OF DIFFERENT F/NF MAPS OF 2010 AND 2015 IN HAINAN ISLAND USING GROUND REFERENCE SITES (GRS)

Year	F/NF Product	GRS	PA (%)	UA (%)	OA (%)
2010	PALSAR/Landsat	Empirical	96.31	99.45	97.35
	JAXA		69.22	98.62	82.42
	FORM-GLC		86.05	95.89	88.38
	GlobeLand30		94.44	90.90	89.72
2015	PALSAR/Landsat	Empirical	94.94	99.62	96.43
		Random	96.58	91.22	92.47

Detailed accuracy assessment of different F/NF maps is presented in Tables S2–S8; PA: Producer's accuracy; UA: User's accuracy; OA: Overall accuracy.

TABLE III
FOREST AREA OF HAINAN ISLAND IN 2010 FROM DIFFERENT DATA SOURCES

	Mapped area (ha)	Adjusted area (ha)
PALSAR/Landsat	2.05×10^6	$2.12 \times 10^6\,(\pm 4231)$
JAXA	1.31×10^6	$1.87 \times 10^6\,(\pm 10\,695)$
FROM-GLC	2.00×10^6	$2.23 \times 10^6\,(\pm 8328)$
GlobeLand30	2.41×10^6	$2.32 \times 10^6\,(\pm 8627)$
NLCD (1 km res.)	2.15×10^6	–
Statistical data	2.04×10^6	–

The adjusted area is derived from an error-adjusted matrix considering user accuracy, and values in bracket are standard deviation.

groups were calculated. Since JAXA annual F/NF maps (2007–2010) were publicly available, the forest dynamics analysis was performed on both F/NF maps of PALSAR/Landsat-based and JAXA, and the results during 2007 and 2010 period from these two products were compared.

III. RESULTS

A. Accuracy Assessment of Forest Cover Maps in 2010 and 2015

Accuracy assessments with GRS showed that the PALSAR/Landsat F/NF maps had the highest accuracy (see Tables II and S2–S8). In 2010, assessments showed that PA, UA, and OA for the PALSAR/Landsat F/NF map were 96.31%, 99.45%, and 97.35%, respectively. This map was followed in order of accuracy by GlobeLand30, FROM-GLC, and JAXA. These F/NF maps hold an OA of 89.72%, 88.38%, and 82.42%, respectively. Among these F/NF maps, the JAXA F/NF map had a high UA of 98.62%, but the lowest PA of 69.22%. In 2015, the PALSAR/Landsat F/NF map shows high accuracy when validated with different GRS. The OA for empirical and random GRS was 96.43% and 92.47%, respectively.

B. Intercomparison Between F/NF Maps of PALSAR/Landsat and JAXA, FROM-GLC, GlobeLand30, and NLCD in 2010

All F/NF maps showed similar distributions of dense forest coverage in the middle mountain areas (see Fig. 5), but had significant differences in the rest of the island. In the northwestern coastline, there was almost no forest in the F/NF maps produced by JAXA and FROM-GLC. In addition, very few forests were observed in the JAXA F/NF map in the central, northeastern, and southeastern regions [see Fig. 5(b)] when compared with the other four F/NF maps. The GlobeLand30 F/NF map showed the densest forest coverage among these five maps, while the PALSAR/Landsat F/NF map and the NLCD had a very similar forest spatial distribution [see Fig. 5(a) and (e)].

The PALSAR/Landsat F/NF map at the county scale is significantly correlated with those of JAXA ($R^2 = 0.84, P < 0.01$), FROM-GLC ($R^2 = 0.82, P < 0.01$), GlobeLand30 ($R^2 = 0.81, P < 0.01$), and NLCD ($R^2 = 0.91, P < 0.01$) with root mean squared error of 21 400, 19 000, 21 300, and 14 500 ha, respectively [see Fig. 5(g)]. The slopes of forest area between PALSAR/Landsat and JAXA, FROM-GLC, GlobeLand30, and NLCD at the county scale are 0.99, 0.84, 0.91, and 0.96, respectively.

Total forest area estimates in 2010 by JAXA were significantly lower than the other of the F/NF maps, with an adjusted area of 1.87×10^6 ($\pm 10\,695$) ha (1.31×10^6 ha mapped area, Table III). The GlobeLand30 map had the largest forest area of $2.3 \times 10^6 (\pm 8627)$ ha (2.41×10^6 ha mapped area), since it estimated more forest in most regions [see Fig. 5(d)]. The adjusted forest area derived from PALSAR/Landsat and FROM-GLC was $2.1 \times 10^6 (\pm 4231)$ and $2.23 \times 10^6 (\pm 8328)$ ha, respectively. The mapped area of NLCD was 2.15×10^6 ha. Among these F/NF maps, the PALSAR/Landsat map had the lowest 95% confidence interval ($\pm$4231 ha) in forest area, and the mapped (2.05×10^6 ha) and adjusted areas were the closest to the statistical data (2.04×10^6 ha) [52].

C. Intercomparison of Annual Forest Dynamics (2007–2010) Between JAXA and PALSAR/Landsat F/NF Maps

Large inconsistencies were found between the PALSAR/Landsat and JAXA F/NF maps for all years in those areas with an elevation less than 400 m [see Fig. 6(a)–(d)]. Above this elevation, the two products had a high degree of consistency: the lower the elevation, the larger the difference between these two maps. Forests in the PALSAR/Landsat maps were mainly distributed in those areas with an elevation of less than 600 m, while most of JAXA's forests were located within those areas at an elevation of 200–800 m. In addition, forest area with an elevation less than 400 m in the JAXA F/NF map in 2009 was significantly higher than the other three years [see Fig. 6(e)]. Less than half of the JAXA forests (about 7.50×10^5 ha) in high elevation mountainous regions were detected as unchanged during 2007 and 2010 [see Fig. 7(a) and (c)]. Most of the remaining pixels were identified as forest one or two times during the four years. The largest agreement between JAXA and PALSAR/Landsat F/NF occurs in 4-year forest pixels [see Fig. 7(d)]. The poor spatial consistency of the JAXA annual F/NF maps indicates that they are unreliable for forest dynamics analysis at low-elevation regions on Hainan Island.

The PALSAR/Landsat F/NF maps illustrated a gradual increase of forests in those areas with an elevation of less than 400 m during 2007 and 2010 [see Fig. 6(f)]. When compared with 2007, 2008, and 2010, slightly more forest was found in 2009 at elevations less than 400 m. Above this elevation, forest areas were almost unchanged. The overlapped PALSAR/Landsat F/NF map between 2007 and 2010 showed very good consistency [see Fig. 7(b)]. The stable forest area was about 1.8 million ha and mainly distributed in mountainous regions and surrounding lowlands [see Fig. 7(b) and (c)].

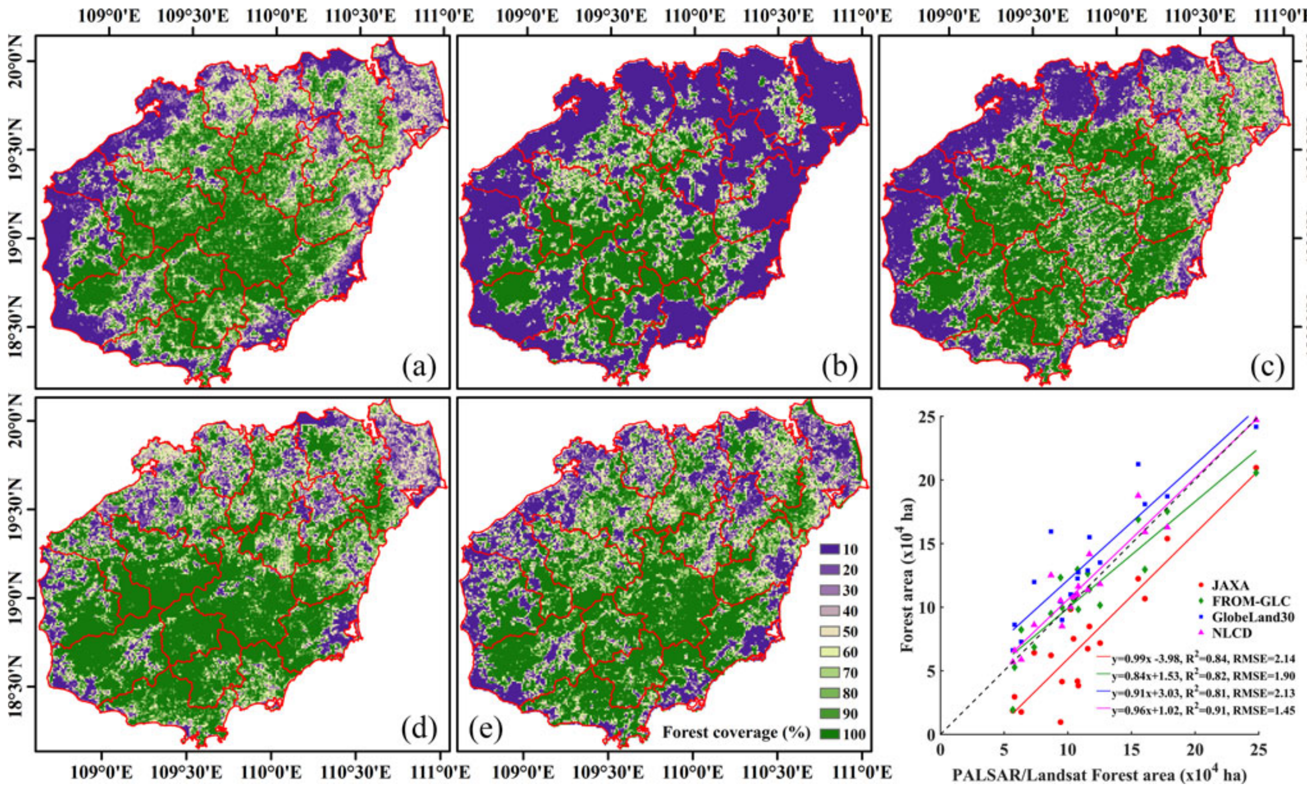

Fig. 5. Forest cover maps of (a) PALSAR/Landsat, (b) JAXA, (c) FROM-GLC, (d) GlobeLand30, (e) NLCD at 1-km spatial resolution of Hainan Island in 2010, and (g) regression plots of PALSAR/Landsat forest area against forest area of JAXA, FROM-GLC, GlobeLand30, and NLCD at county scale.

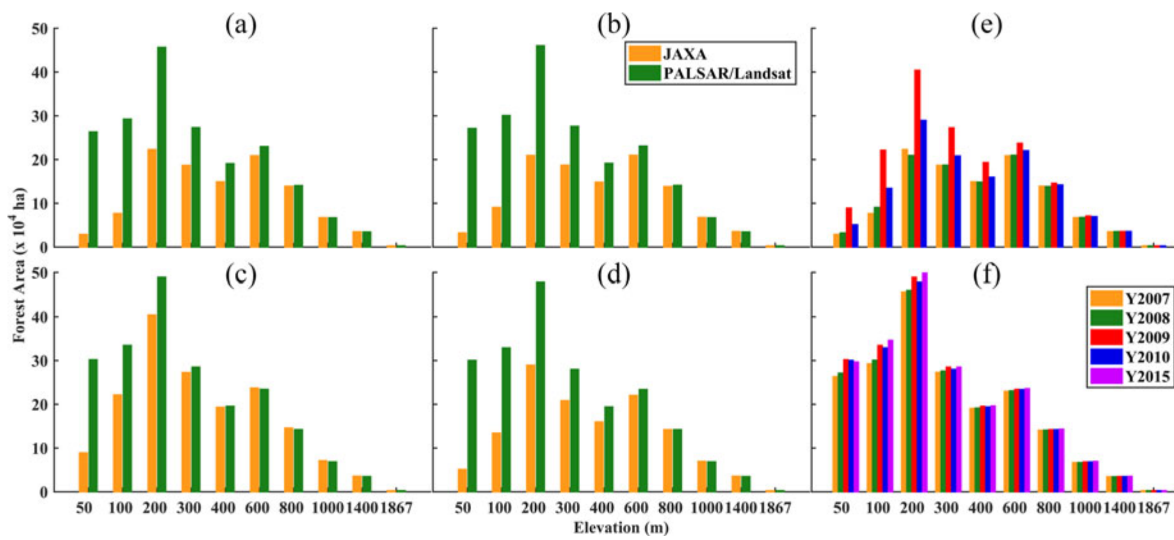

Fig. 6. Forest area dynamic comparisons at different elevations on Hainan Island, China, based on the JAXA and PALSAR/Landsat F/NF maps for (a) 2007, (b) 2008, (c) 2009, (d) 2010, and grouped forest dynamic for (e) JAXA (2007–2010), and (f) PALSAR/Landsat (2007–2010, 2015), respectively.

D. Forest Dynamic on Hainan Island Between 2007 and 2015 From PALSAR/Landsat F/NF Maps

The annual PALSAR/Landsat F/NF maps from 2007 to 2015 had good spatial consistency (see Fig. 8). Due to less rainfall and a dry climate, very few forests are distributed in the western regions. Few changes were found from 2007 to 2010, but more evident changes were found in the west-central, northcentral, and northeast between 2010 and 2015 (see Fig. 8). The stable forest area from 2007 to 2015 accounts for 70.68% of the total forest area. Total mapped forest areas on Hainan Island were 1.87 million, 1.92 million, 2.05 million, 2.05 million, and 2.12 million ha, for 2007, 2008, 2009, 2010, and 2015, respectively.

Fig. 9 shows the spatial distribution of forest gain and loss between 2007 and 2015. The stable forest area from 2007 to 2015 accounted for 50.89% of the total island land area. Reforestation/afforestation is more dramatic in the western and northern regions (zoom view I in Fig. 9) and forest gain accounted for 12.65% of the total island land area. High forest gain (162 300

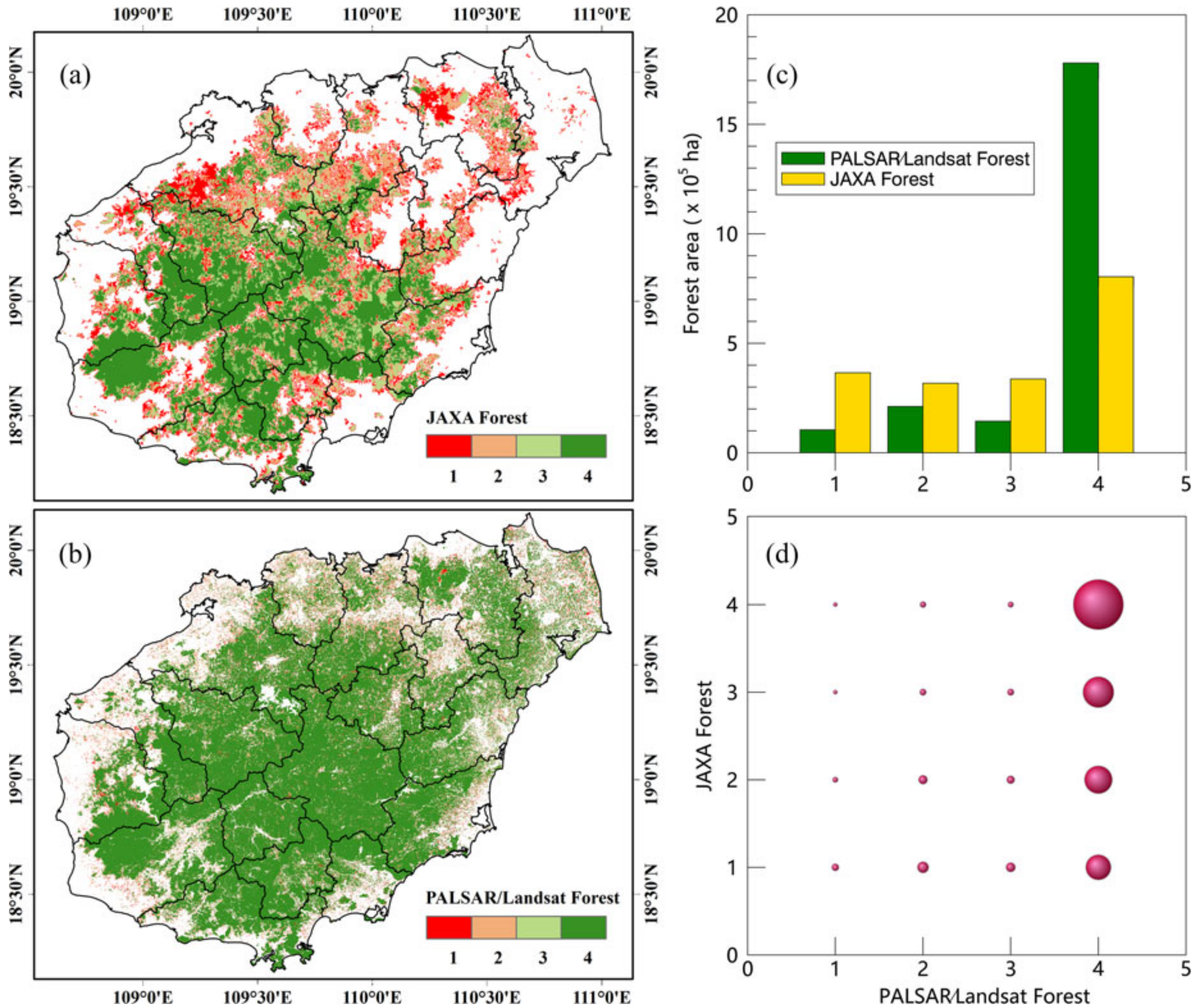

Fig. 7. Forest spatial dynamic comparison on Hainan Island, China: (a) overlapped map from 2007 to 2010 JAXA F/NF maps, (b) overlapped map from 2007 to 2010 PALSAR/Landsat F/NF maps, (c) area bar plot of forest convention between PALSAR/Landsat and JAXA F/NF maps, and (d) bubble plot of forest convention between PALSAR/Landsat and JAXA maps. The numbers (1–4) in the legends of (a) and (b) and coordinates of (c) and (d) represent the number of years a pixel was identified as forest during 2007–2010. Bubble size corresponds to the forest area.

ha) was found from 2008 to 2009, while gains from 2007 to 2008 and from 2009 to 2010 ranged from 74 079 to 90 835 ha (see Table IV). Total forest gain was 207 927 ha for 2010 to 2015 and 414 568 ha for 2007 to 2015. In addition to a net forest loss (2333 ha) from 2009 to 2010, net forest gains were found for the remaining. The total net forest gain from 2007 to 2015 was 235 921 ha, about 26 213 ha (1.23%) per year.

Forest loss occurred mainly in northeastern regions like Haikou and Wenchang city (zoom view III in Fig. 9) and its area accounted for 5.45% of the total island land area. The annual forest loss area between 2007 and 2010 ranged from 30 254 to 76 412 ha and total forest loss between 2007 and 2015 was 178 647 ha (see Table IV). Consistent nonforest accounted for 31.01% of the island's land cover and was mainly distributed in regions close to the coastlines [see Fig. 9(I)].

About than 95% of forest gain and loss from 2007 to 2015 happened at an elevation of less than 400 m, and slight gains and losses occurred at elevations between 400 and 800 m (see Table V). About 99% of the forest was unchanged above an elevation of 800 m. The proportion of forest gain above 50 m elevation is slightly larger than the proportion of forest loss.

TABLE IV
FOREST LOSS AND GAIN BETWEEN 2007 AND 2015 (IN HA)

	Gains	Losses	Net change
2007–2008	90 835	43 542	47 293
2008–2009	162 300	30 254	132 046
2009–2010	74 079	76 254	–2333
2010–2015	207 927	148 658	59 269
2007–2015	414 568	178 647	235 921

More than 95% of net forest gain is observed at regions with elevation less than 600 m.

IV. Discussion

A. Forest Mapping Using PALSAR/PALSAR-2 and Time Series Optical Images

The L-band PALSAR/PALSAR-2 and time series optical imagery has been increasingly used for forest mapping in recent years [6], [25], [33], [35], [53]. Our optical–SAR-based forest mapping algorithm has been successfully applied in Mainland

This article has been accepted for inclusion in a future issue of this journal. Content is final as presented, with the exception of pagination.

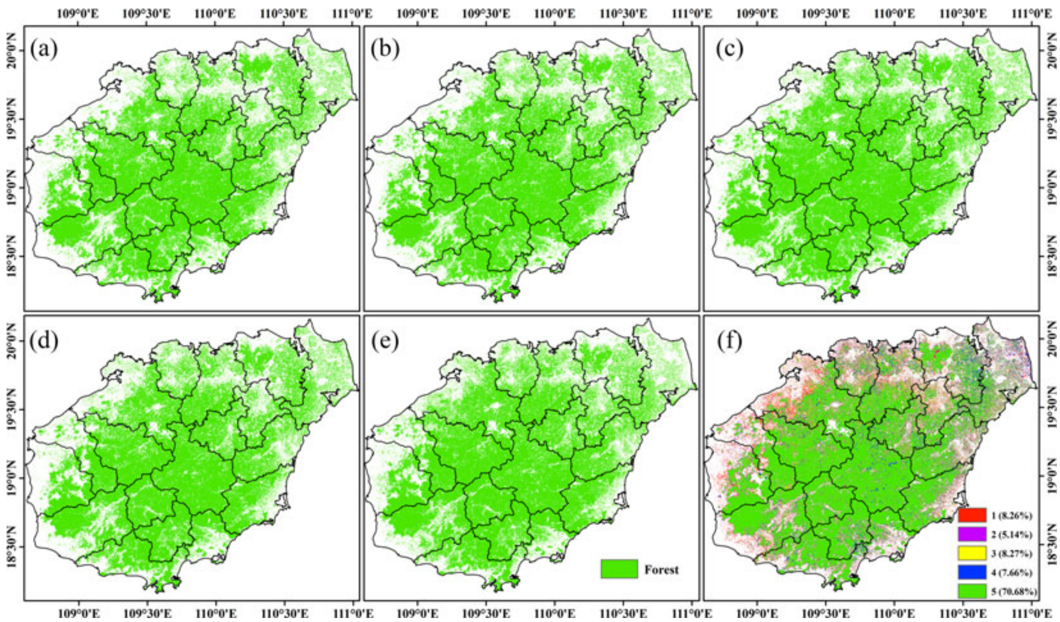

Fig. 8. Spatial distribution of PALSAR/Landsat F/NF maps of Hainan Island: (a) 2007, (b) 2008, (c) 2009, (d) 2010, (e) 2015, and (f) overlapped map from 2007 to 2015 PALSAR/Landsat F/NF maps. In legends, 1–5 (f) represent the number of years a pixel was identified as forest during 2007–2015, and the percentage values were their proportion to the total forest area.

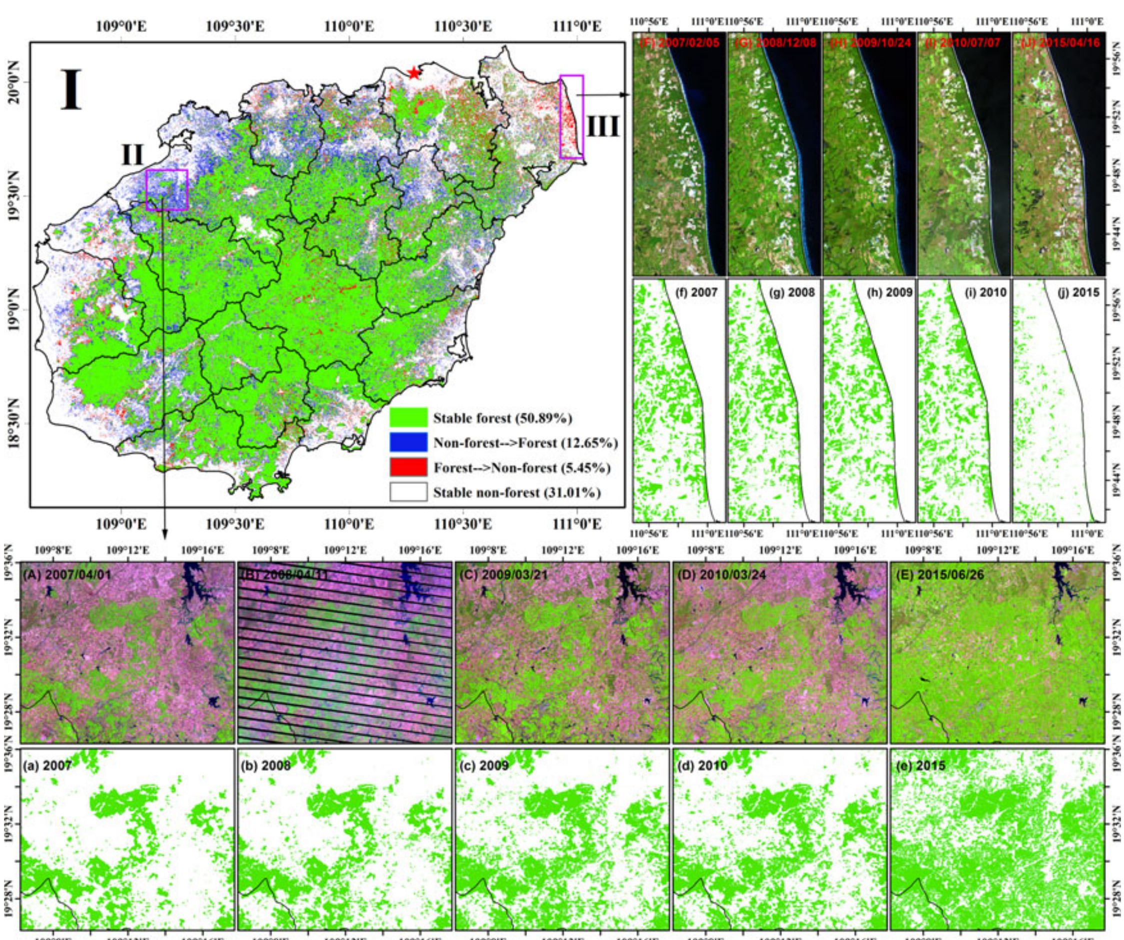

Fig. 9. Spatial distribution of forest gain and loss during 2007–2015 on Hainan Island: (I) aggregated forest loss and gain, (A–E) illustration of forest gain hot spot due to rubber plantation expansion in Danzhou city (zoom extent II) shown in Landsat TM/ETM/OLI false color composite, and (a)–(e) corresponding F/NF map of (A)–(E). Forest is shown in green. (F)–(J) Illustration of forest loss hot spot in Wenchang City (zoom extent III) shown in false color composite of Landsat TM/ETM+/OLI imagery, and (f)–(j) corresponding F/NF maps of (F)–(J).

This article has been accepted for inclusion in a future issue of this journal. Content is final as presented, with the exception of pagination.

TABLE V
STATISTICAL INFORMATION OF FOREST DYNAMICS AT DIFFERENT ELEVATIONS IN HAINAN ISLAND DURING 2007 AND 2015

	0–50 m	50–100 m	100–200 m	200–300 m	300–400 m	400–600 m	600–800 m	800–1000 m	1000–1400 m	1400–1867 m
Loss (ha/%)	70 892/40.0	40 903/23.1	41 413/23.4	13 297/7.5	5512/3.1	3217/1.8	1218/0.7	445/0.3	176/0.1	16/0.01
Gain (ha/%)	130 427/31.4	110 211/26.6	101 877/24.5	35 114/8.5	16 016/3.9	12 010/2.9	4972/1.2	3532/0.9	936/0.2	66/0.02
Net change (ha/%)	59 535/25.0	69 308/29.1	60 464/25.4	21 817/9.2	10 504/4.4	8793/3.7	3754/1.6	3087/1.3	760/0.3	50/0.02

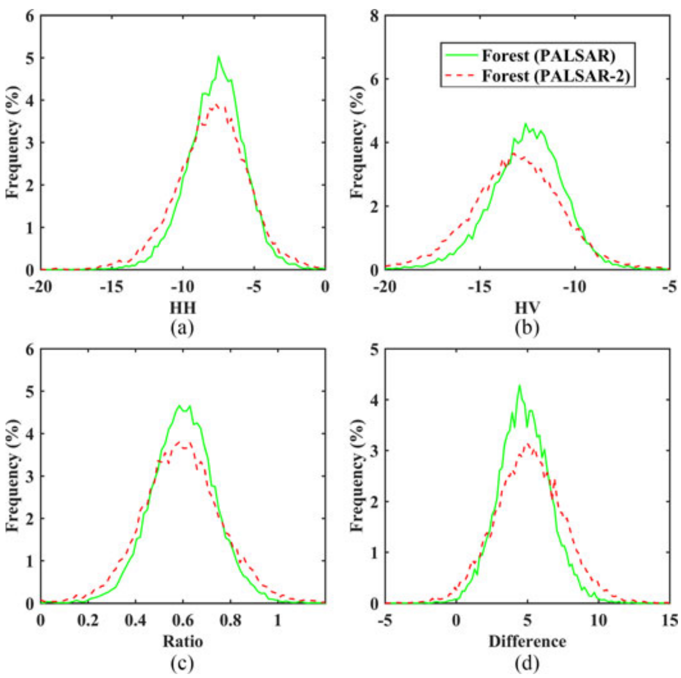

Fig. 10. Signature difference of forest between PALSAR and PALSAR-2 based on forest GRS of 2010 and 2015, respectively: (a) HH, (b) HV, (c) ratio (HH/HV), and (d) difference (HH – HV).

Southeast Asia [30], China [31], and monsoon Asia [54] with 50 m PALSAR and MODIS data. When the 25 m PALSAR dataset was available in 2014, we extended this algorithm in Hainan Island, China [35] and Oklahoma, USA [37] with 25 m PALSAR and Landsat TM/ETM+ imagery. With the release of PALSAR-2 global mosaic data in 2016, we found that it has good consistency with PALSAR data (see Figs. S3 and S5), and our PALSAR/Landsat-based forest mapping algorithm can be applied to PALSAR-2 and time series Landsat ETM+/OLI imagery. The slight left shift of forest HH and HV values in PALSAR-2 over that of PALSAR (see Fig. 10) can be attributed to the difference in sensors, image acquisition time, and GRS. With the powerful GEE cloud computing platform and cost-free data policy, it is easy to implement this algorithm to track tropical forest dynamics (2007–2010, 2015 onwards) at large scales. However, the thresholds for forest mapping using PALSAR-2 data in other regions should be further evaluated.

In previous studies, we found that commission errors were serious in urban regions due to similar backscatter coefficients of PALSAR between forest and built-up, and therefore used $\text{NDVI}_{\max}$ from MODIS [54] and Landsat [35] to eliminate those misclassified pixels in PALSAR-based F/NF maps. In this study, high biomass crops such as sugarcane and banana plantations were found to have similar backscatter coefficients as forest, too [see Fig. 4(c) and (d)]. Others also found that PALSAR radar signals increased quickly with sugarcane plant height until a threshold height of about 2.3 m [55]. Most cultivated banana plants can reach 5 m tall and are sometimes referred to as banana trees. These high biomass crops were likely to be misclassified as forest if PALSAR/PALSAR-2 acquisition dates correspond to crop maturity and high biomass dates. For example, the second PALSAR strip on left in 2009 was acquired on September 15 [see Fig. 1(b)], which was during the season that both sugarcane and banana have high biomass. This strip was captured in a region that has the densest banana and sugarcane crops [39]. The commission error was serious in PALSAR-based F/NF map [see Fig. 11(b)], and that was why the forest area in JAXA PALSAR-based F/NF map of 2009 in regions with elevation less than 400 m was significantly higher than those of the remaining three years [see Fig. 6(e)]. The proposed harvest frequency criteria (F_{Harvest}, NDVI < 0.5, and LSWI < 0.1) applied to time series Landsat images that were acquired from periods of harvest to early crop rotation showed good performance in eliminating commission errors of these high biomass crops [see Figs. 11(d) and 6(f)]. Our optical/SAR-based forest maps have good consistency at different elevations and across several years. Introducing F_{Harvest} has generated a more accurate F/NF map for 2010 (OA $= 97.2\%$) than our previous study (OA $= 96.8\%$) [35], and eliminated about 60 000 ha of high biomass crops (forest area decreased from 2.11 to 2.05 million ha). Based on these analyses, we recommend that the image acquisition dates be considered in the context of crop type, phenology, and biomass dynamics in a study area before mapping with the PALSAR/PALSAR-2 data.

A slight overestimation of forest area was found in 2009 in regions with elevations less than 400 m, even when filtering with $F_{\text{Harvest}} < 5\%$ [see Fig. 6(f)]. The overestimation led to a high forest gain (162 300 ha) from 2008 to 2009 and net forest loss (2333 ha) from 2009 to 2010. This overestimation may be caused by the existence of high biomass banana plantations in September [see Fig. 12(c)], which have high NDVI and LSWI values, therefore cannot be removed by rule of $F_{\text{Harvest}} < 5\%$ [see Fig. 12(e)]. On Hainan Island, most banana plants are antiseason with harvest occurring between May and July to avoid an overlapping harvest with banana in mainland China. Unlike sugarcane, whose complete biomass is harvested each year, a complete removal of banana plant biomass usually takes 2–3 years since farmers continue rotation with offshoots that developed from base. Therefore, it is not easy to eliminate banana plantations harvested between May and July with limited cloud-free optical images, if they were already classified as forest by PALSAR/PALSAR-2 images.

In addition, some eucalyptus plantations along the western coastline have almost no understory due to the salty and infertile soil and dry climate [see Fig. 12(d)]. These plantations

This article has been accepted for inclusion in a future issue of this journal. Content is final as presented, with the exception of pagination.

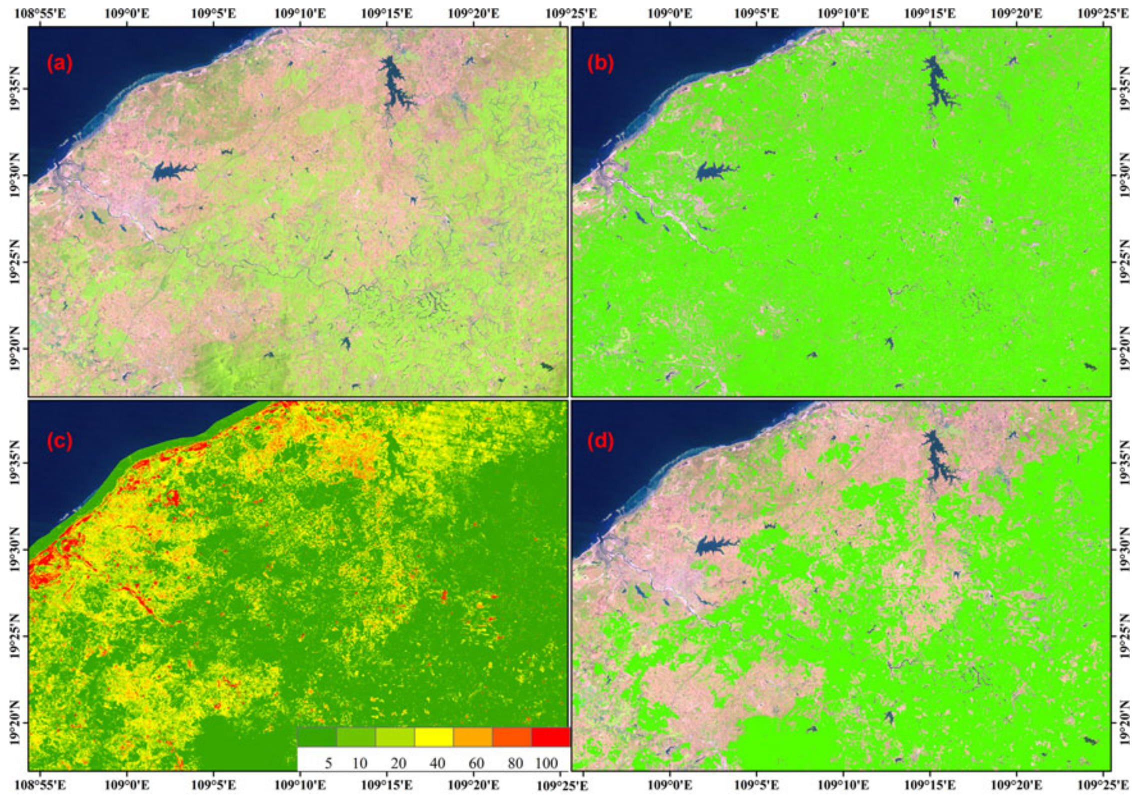

Fig. 11. Schematic of removing high biomass corps in PALSAR-based F/NF map based on the frequency criteria of NDVI < 0.5 and LSWI $< 0.1 (F_{\text{Harvest}})$: (a) False color composite of Landsat TM imagery on 03/24/2010 (R/G/B = band 5/4/3) in western region of Hainan Island, China, (b) PALSAR-based F/NF map in 2009 after $\text{NDVI}_{\max}$ filtering, (c) spatial distribution of F_{Harvest} derived from TM/ETM+ images acquired during 2008–2009 and day-of-year between 90 and 365, and (d) PALSAR/Landsat F/NF map derived from PALSAR-based F/NF map after $\text{NDVI}_{\max} > 0.65$ and $F_{\text{Harvest}} < 5\%$ filtration.

sometimes have much lower values of NDVI and LSWI, especially in the dry season [see Fig. 12(f)], and were removed by the $F_{\text{Harvest}} < 5\%$ threshold even though they were classified as forest by PALSAR/PALSAR-2 data. Therefore, we have slightly underestimated the forest area in arid regions along the western coast. To avoid large areas of underestimation, studies should consider the climate and forest conditions of a study area when applying our algorithm to other regions.

B. Comparison Between PALSAR/Landsat and Other Optical-Based F/NF Maps

The PALSAR/Landsat F/NF map in 2010 had a good agreement with the F/NF maps of FROM-GLC, GlobeLand30, and NLCD for most of the island [see Fig. 5(c)–(e)]. Forest area from the PALSAR/Landsat F/NF maps was significantly correlated with that of the optical-based F/NF maps at the county scale ($R^2 = 0.81$–0.91). At the 30 m scale, the PALSAR/Landsat F/NF had higher accuracy (OA $> 96\%$) than the optical-based F/NF maps from FROM-GLC and GlobeLand30 (OA $= 88$–90%) (see Table II). The good performance of PALSAR/Landsat F/NF map is due to the incorporation of both optical and SAR data. The differences among the PALSAR/Landsat, FROM-GLC, and GlobeLand30 F/NF maps, and NLCD can be explained by forest definition, data source, and the algorithms used for mapping [31]. For example, the FROM-GLC F/NF map was generated using a random forest method of classification [20], and the GlobeLand30 was derived from pixel- and object-based methods with a knowledge approach with a minimum mapping unit of 8×8 30 m pixels for forest [10], while the NLCD was mainly obtained using a human–computer interactive method [56].

C. Forest Dynamic on Hainan Island During 2007 and 2015

The PALSAR data were stable during 2007 and 2010 (see Fig. S5) and PALSAR-2 was consistent with its predecessor. Thus, the annual PALSAR/Landsat forest maps derived from the algorithm can serve as a reliable data source for annual forest dynamic analysis (see Table II and Fig. 8). Forest gain from 2007 to 2015 was mainly due to the expansion of industrial plantations such as natural rubber, eucalyptus, and orchard. The dense forest gains (in blue) along the western and northern areas of the island [see Fig. 9(I)] were mainly rubber and eucalyptus because of a favorable climate and environment. In the 2000s, rubber plantations, especially privately owned plantations, increased significantly due to rapid increases in the price of natural rubber [57]. According to the statistical yearbooks, net growth of rubber plantations from 2007 to 2015 was 105 000 ha [39], [58]. Fig. 9(A)–(e) clearly demonstrates the expansion of rubber plantations. Only a few rubber plantations existed in 2007 [see Fig. 9(A)–(a)], and the rubber plantation area increased slightly in 2010 [see Fig. 9(C)–(c)], but almost completely covered this region in 2015 [see Fig. 9(D)–(d)]. In addition, eucalyptus plantations on Hainan Island have increased significantly since 1997, when policies began to encourage eucalyptus plantations for industrial use. The area of eucalyptus plantations reached 100 000

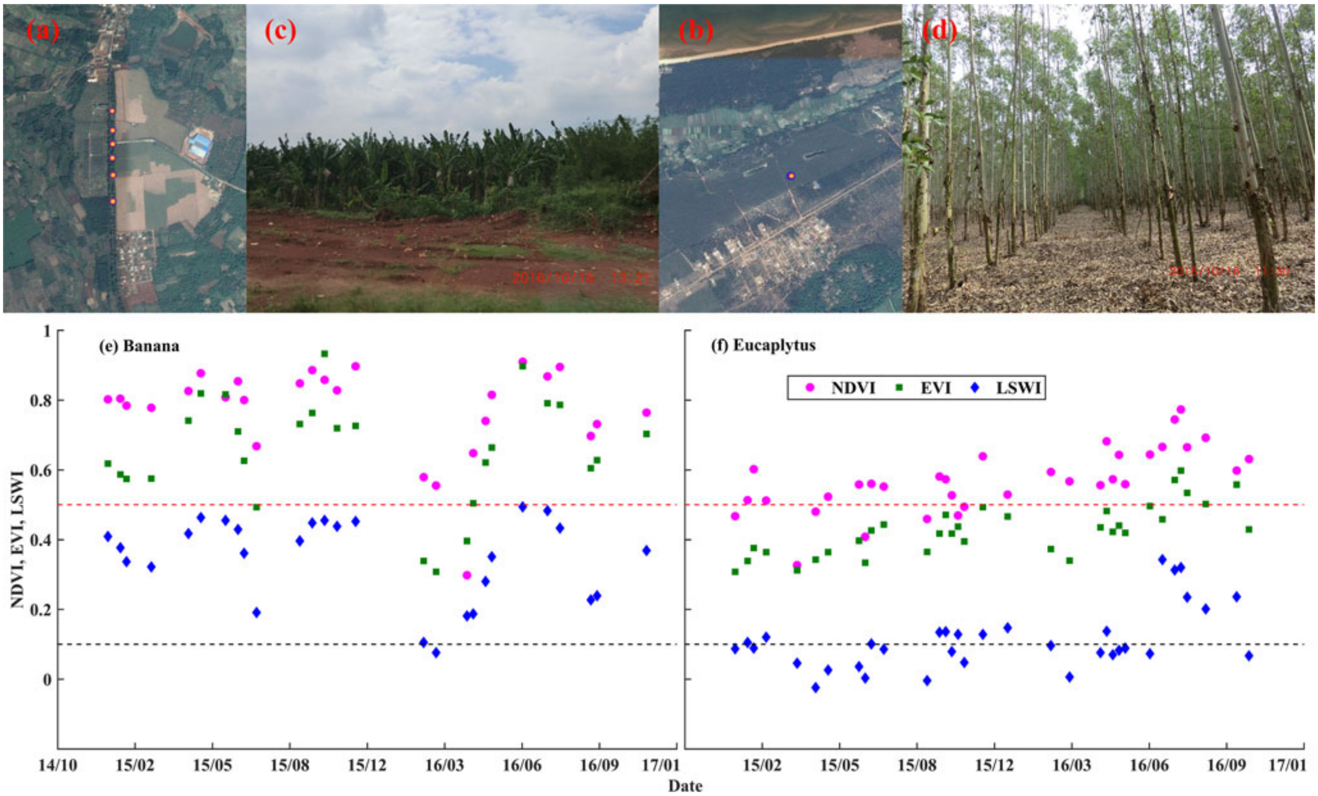

Fig. 12. Illustration of uncertainties from banana plantations not harvest during May to July and eucalyptus plantation without understory: (a) and (b) spatial distribution of banana (19.8137 °N, 109.6848 °E) and eucalyptus (19.5049 °N, 109.8355 °E) plantations from Google VHSR images, respectively; (c) and (d) field photos of corresponding banana and eucalyptus plantations taken on October 16, 2016, respectively; (e) and (f) NDVI, EVI, and LSWI time series of corresponding banana and eucalyptus plantations from January 1, 2015 to December 31, 2016, respectively.

ha in 2006 and continued to increase by ∼(25 000–40 000) ha per year [59].

Forest losses can be attributed to urbanization, removing old rubber plantations, and regular harvesting of eucalyptus plantations. The northeastern corner of Hainan Island (The capital Haikou and Wenchang City), for example, experienced dramatic deforestation in recent years due mainly to urbanization, such as of hotel and resort construction and the development of real estate [see Figs. 9(G)–(j) and S9]. In addition, about 170 000 ha rubber plantations have been planted between 1975 and 1990 [60]. These plantations have been gradually removed after 2005 because rubber trees have an economic life cycle of about 25–35 years. In addition, the elevations at which more than 95% forest gains and losses (see Table IV) are concentrated (<400 m) are quite consistent with the recommended elevation (<350 m) for rubber tree plantations on Hainan Island [61]. The expansion of rubber and eucalyptus plantations on the island contributed substantially to the observed increase of forest cover in this study.

V. Conclusion

In this study, we found that the forest mapping algorithm based on ALOS PALSAR and time series Landsat TM/ETM+ imagery can be readily applied to ALOS2 PALSAR-2 and time series Landsat ETM+/OLI imagery. The PALSAR-2, PALSAR, and Landsat series data have good consistency, so a uniform algorithm can be used to track forest dynamics in the tropics. In addition, we found that high biomass crops like sugarcane and banana plantations may be misclassified as forest if only L-band SAR imagery is used in the seasons when crops have high biomass. However, these commission errors can be effectively eliminated using the phenology-based metrics derived from the time series Landsat imagery using crop harvest frequency map. By integrating the ALOS/ALOS-2 L-band SAR and time series Landsat TM/ETM+/OLI imagery, annual forest maps of Hainan Island from 2007 to 2015 (OA = 92–97%) were obtained. The area of forest gain, loss, and net change on Hainan Island during 2007 and 2015 was 415 000 ha (+2.17% yr^{-1}), 179 000 ha (–0.94% yr^{-1}), and 236 000 ha (+1.23% yr^{-1}), respectively. Over 95% of the forest gain and loss occurred in those areas with an elevation less than 400 m, due mainly to the expansion of rubber and eucalyptus plantations as well as urbanization. In summary, this study has demonstrated the potential of integrating 25 m ALOS/ALOS-2 and time series Landsat imagery for the purposes of quantifying annual forest dynamics in tropical regions. Future efforts are needed to apply and evaluate the algorithms to track and monitor tropical forest dynamics in other tropical regions.

Acknowledgment

The authors thank the U.S. Geological Survey EROS Data Center, Japan Aerospace Exploration Agency, Tsinghua University, National Geomatics Center of China, and Data Center for Resources and Environmental Sciences, Chinese Academy of Sciences for their images or land cover products, and thanks to Dr. Xueyang and Y. Zhou at Hainan Forestry Department for providing part of the field data. The authors also thank S. Xiao at Yale University and N. Cejda and B. Alikhani at the University of Oklahoma for English language editing of the manuscript.

REFERENCES

[1] J. Lelieveld *et al.*, "Atmospheric oxidation capacity sustained by a tropical forest," *Nature*, vol. 452, no. 7188, pp. 737–740, 2008.
[2] F. Achard *et al.*, "Estimating tropical deforestation from Earth observation data," *Carbon Manage.*, vol. 1, no. 2 pp. 271–287, 2010.
[3] J. Reiche, J. Verbesselt, D. Hoekman, and M. Herold, "Fusing Landsat and SAR time series to detect deforestation in the tropics," *Remote Sens. Environ.*, vol. 156, pp. 276–293, 2015.
[4] G. R. van der Werf *et al.*, "CO2 emissions from forest loss," *Nature Geosci.*, vol. 2, no. 11, pp. 737–738, 2009.
[5] Z. Li and J. M. Fox, "Integrating *Mahalanobis typicalities* with a neural network for rubber distribution mapping," *Remote Sens. Lett.*, vol. 2, no. 2, pp. 157–166, 2011.
[6] T. Motohka, M. Shimada, Y. Uryu, and B. Setiabudi, "Using time series PALSAR gamma nought mosaics for automatic detection of tropical deforestation: A test study in Riau, Indonesia," *Remote Sens. Environ.*, vol. 155, pp. 79–88, 2014.
[7] R. J. Keenan, G. A. Reams, F. Achard, J. V. de Freitas, A. Grainger, and E. Lindquist, "Dynamics of global forest area: Results from the FAO global forest resources assessment 2015," *Forest Ecol. Manage.*, vol. 352, pp. 9–20, 2015.
[8] Y. Yang, P. Xiao, X. Feng, and H. Li, "Accuracy assessment of seven global land cover datasets over China," *ISPRS J. Photogramm.*, vol. 125, pp. 156–173, 2017.
[9] M. C. Hansen *et al.*, "High-resolution global maps of 21st-century forest cover change," *Science*, vol. 342, no. 6160, pp. 850–853, 2013.
[10] J. Chen *et al.*, "Global land cover mapping at 30 m resolution: A POK-based operational approach," *ISPRS J. Photogramm.*, vol. 103, pp. 7–27, 2015.
[11] T. Hermosilla, M. A. Wulder, J. C. White, N. C. Coops, and G. W. Hobart, "Regional detection, characterization, and attribution of annual forest change from 1984 to 2012 using Landsat-derived time-series metrics," *Remote Sens. Environ.*, vol. 170, pp. 121–132, 2015.
[12] M. Vollmar, R. Rasi, R. Beuchle, D. Simonetti, H. Stibig, and F. Achard, "Combining Landsat TM/ETM+ and ALOS AVNIR-2 satellite data for tropical forest cover change detection," *IEEE J. Sel. Topics Appl. Earth Observ. Remote Sens.*, vol. 6, no. 1, pp. 102–109, Feb. 2013.
[13] M. C. Hansen, R. S. DeFries, J. R. G. Townshend, M. Carroll, C. Dimiceli, and R. A. Sohlberg, "Global percent tree cover at a spatial resolution of 500 meters: First results of the MODIS vegetation continuous fields algorithm," *Earth Interact.*, vol. 7, no. 10, pp. 1–15, 2003.
[14] M. A. Friedl *et al.*, "Global land cover mapping from MODIS: Algorithms and early results," *Remote Sens. Environ.*, vol. 83, no. 1, pp. 287–302, 2002.
[15] P. Mayaux and E. F. Lambin, "Tropical forest area measured from global land-cover classifications: Inverse calibration models based on spatial textures," *Remote Sens. Environ.*, vol. 59, no. 1, pp. 29–43, 1997.
[16] M. C. Hansen *et al.*, "Humid tropical forest clearing from 2000 to 2005 quantified by using multitemporal and multiresolution remotely sensed data," *Proc. Nat. Acad. Sci. USA*, vol. 105, no. 27, pp. 9439–9444, 2008.
[17] J. O. Sexton *et al.*, "Global, 30-m resolution continuous fields of tree cover: Landsat-based rescaling of MODIS vegetation continuous fields with LIDAR-based estimates of error," *Int. J. Digit. Earth*, vol. 6, no. 5, pp. 427–448, 2013.
[18] F. Achard *et al.*, "Determination of tropical deforestation rates and related carbon losses from 1990 to 2010," *Global Change Biol.*, vol. 20, no. 8, pp. 2540–2554, 2014.
[19] Z. Oumar and O. Mutanga, "Integrating environmental variables and WorldView-2 image data to improve the prediction and mapping of *Thaumastocoris peregrinus* (bronze bug) damage in plantation forests," *ISPRS J. Photogramm.*, vol. 87, pp. 39–46, 2014.
[20] P. Gong *et al.*, "Finer resolution observation and monitoring of global land cover: First mapping results with Landsat TM and ETM+ data," *Int. J. Remote Sens.*, vol. 34, no. 7, pp. 2607–2654, 2013.
[21] Z. Zhu, S. Wang, and C. E. Woodcock, "Improvement and expansion of the Fmask algorithm: Cloud, cloud shadow, and snow detection for Landsats 4–7, 8, and Sentinel 2 images," *Remote Sens. Environ.*, vol. 159, pp. 269–277, 2015.
[22] G. Vaglio Laurin *et al.*, "Optical and SAR sensor synergies for forest and land cover mapping in a tropical site in West Africa," *Int. J. Appl. Earth Observ.*, vol. 21, pp. 7–16, 2013.
[23] J. Dong *et al.*, "A 50-m forest cover map in Southeast Asia from ALOS/PALSAR and its application on forest fragmentation assessment," *PLoS One*, vol. 9, no. 1, 2014, Art. no. e85801.
[24] R. B. Thapa, T. Itoh, M. Shimada, M. Watanabe, M. Takeshi, and T. Shiraishi, "Evaluation of ALOS PALSAR sensitivity for characterizing natural forest cover in wider tropical areas," *Remote Sens. Environ.*, vol. 155, pp. 32–41, 2014.
[25] M. Shimada *et al.*, "New global forest/non-forest maps from ALOS PALSAR data (2007–2010)," *Remote Sens. Environ.*, vol. 155, pp. 13–31, 2014.
[26] H. Jin, G. Mountrakis, and S. V. Stehman, "Assessing integration of intensity, polarimetric scattering, interferometric coherence and spatial texture metrics in PALSAR-derived land cover classification," *ISPRS J. Photogramm.*, vol. 98, pp. 70–84, 2014.
[27] M. Whittle, S. Quegan, Y. Uryu, M. Stüewe, and K. Yulianto, "Detection of tropical deforestation using ALOS-PALSAR: A Sumatran case study," *Remote Sens. Environ.*, vol. 124, pp. 83–98, 2012.
[28] S. Mermoz and T. Le Toan, "Forest disturbances and regrowth assessment using ALOS PALSAR data from 2007 to 2010 in Vietnam, Cambodia and Lao PDR," *Remote Sens.*, vol. 8, no. 3, 2016, Art. no. 217.
[29] N. Joshi *et al.*, "Mapping dynamics of deforestation and forest degradation in tropical forests using radar satellite data," *Environ. Res. Lett.*, vol. 10, no. 3, 2015, Art. no. 34014.
[30] J. Dong, X. Xiao, S. Sheldon, C. Biradar, N. D. Duong, and M. Hazarika, "A comparison of forest cover maps in Mainland Southeast Asia from multiple sources: PALSAR, MERIS, MODIS and FRA," *Remote Sens. Environ.*, vol. 127, pp. 60–73, 2012.
[31] Y. Qin *et al.*, "Forest cover maps of China in 2010 from multiple approaches and data sources: PALSAR, Landsat, MODIS, FRA, and NFI," *ISPRS J. Photogramm.*, vol. 109, pp. 1–16, 2015.
[32] E. A. Lehmann *et al.*, "SAR and optical remote sensing: Assessment of complementarity and interoperability in the context of a large-scale operational forest monitoring system," *Remote Sens. Environ.*, vol. 156, pp. 335–348, 2015.
[33] J. Dong *et al.*, "Mapping deciduous rubber plantations through integration of PALSAR and multi-temporal Landsat imagery," *Remote Sens. Environ.*, vol. 134, pp. 392–402, 2013.
[34] R. Jhonnerie, V. P. Siregar, B. Nababan, L. B. Prasetyo, and S. Wouthuyzen, "Random forest classification for mangrove land cover mapping using landsat 5 TM and Alos PALSAR imageries," *Proc. Environ. Sci.*, vol. 24, pp. 215–221, 2015.
[35] B. Chen *et al.*, "Mapping tropical forests and deciduous rubber plantations in Hainan Island, China by integrating PALSAR 25-m and multi-temporal Landsat images," *Int. J. Appl. Earth Observ.*, vol. 50, pp. 117–130, 2016.
[36] J. G. Masek *et al.*, "LEDAPS calibration, reflectance, atmospheric correction preprocessing code, version 2," ORNL DAAC, Oak Ridge, TN, USA, 2013.
[37] Y. Qin *et al.*, "Mapping annual forest cover in sub-humid and semi-arid regions through analysis of Landsat and PALSAR imagery," *Remote Sens.*, vol. 8, no. 11, 2016, Art. no. 933.
[38] J. Huang, *Study on Sustainable Management of Tropical Forest in Hainan Island*. China, Beijing: Chin. Acad. Forestry, 2006, p. 142.
[39] Statist. Bureau Hainan Province, Surv. Office Nat. Bureau Statist. Hainan, *Hainan Statistical Yearbook 2015*. China, Beijing: China Statist. Press, 2015.
[40] Earth Observ. Res. Center, Jpn. Aerosp. Explor. Agency, "Global 25 m resolution PALSAR-2/PALSAR mosaic and forest/non-forest map (FNF) dataset description," Tokyo, Japan, 2017.
[41] United States Geol. Surv., "Provisional Landsat 8 surface reflectance code (LASRC) product," Reston, VA, USA, 2016.
[42] C. J. Tucker, "Red and photographic infrared linear combinations for monitoring vegetation," *Remote Sens. Environ.*, vol. 8, no. 2, pp. 127–150, 1979.
[43] A. Huete, K. Didan, T. Miura, E. P. Rodriguez, X. Gao, and L. G. Ferreira, "Overview of the radiometric and biophysical performance of the MODIS vegetation indices," *Remote Sens. Environ.*, vol. 83, nos. 1–2, pp. 195–213, 2002.

[44] X. Xiao *et al.*, "Satellite-based modeling of gross primary production in an evergreen needle leaf forest," *Remote Sens. Environ.*, vol. 89, no. 4, pp. 519–534, 2004.
[45] B. Gao, "NDWI—A normalized difference water index for remote sensing of vegetation liquid water from space," *Remote Sens. Environ.*, vol. 58, no. 3, pp. 257–266, 1996.
[46] R. A. Schowengerdt, *Remote Sensing: Models and Methods for Image Processing*, 3 ed. New York, NY, USA: Academic, 2006, p. 515.
[47] Food Agric. Org. U.N., "Global forest resources assessment 2010," Rome, Italy, 2010.
[48] X. Xiao *et al.*, "Mapping paddy rice agriculture in southern China using multi-temporal MODIS images," *Remote Sens. Environ.*, vol. 95, no. 4, pp. 480–492, 2005.
[49] P. Olofsson, G. M. Foody, M. Herold, S. V. Stehman, C. E. Woodcock, and M. A. Wulder, "Good practices for estimating area and assessing accuracy of land change," *Remote Sens. Environ.*, vol. 148, pp. 42–57, 2014.
[50] S. B. Jeon, P. Olofsson, and C. E. Woodcock, "Land use change in New England: A reversal of the forest transition," *J. Land Use Sci.*, vol. 9, no. 1, pp. 105–130, 2012.
[51] P. Olofsson, G. M. Foody, S. V. Stehman, and C. E. Woodcock, "Making better use of accuracy data in land change studies: Estimating accuracy and area and quantifying uncertainty using stratified estimation," *Remote Sens. Environ.*, vol. 129, pp. 122–131, 2013.
[52] Statist. Bureau Hainan Province, Surv. Office Nat. Bureau Statist. Hainan, *Hainan Statistical Yearbook 2011*. China, Beijing: China Statist. Press, 2011.
[53] V. Liesenberg and R. E. Gloaguen, "SAR polarization modes at L-band for forest classification purposes in Eastern Amazon, Brazil," *Int. J. Appl. Earth Observ.*, vol. 21, pp. 122–135, 2013.
[54] Y. Qin *et al.*, "Mapping forests in monsoon Asia with ALOS PALSAR 50-m mosaic images and MODIS imagery in 2010," *Sci. Rep.*, vol. 6, 2016, Art. no. 20880.
[55] N. Baghdadi, N. Boyer, P. Todoroff, M. El Hajj, and A. Bégué, "Potential of SAR sensors TerraSAR-X, ASAR/ENVISAT and PALSAR/ALOS for monitoring sugarcane crops on Reunion Island," *Remote Sens. Environ.*, vol. 113, no. 8, pp. 1724–1738, 2009.
[56] J. Liu *et al.*, "Spatial and temporal patterns of China's cropland during 1990–2000: An analysis based on Landsat TM data," *Remote Sens. Environ.*, vol. 98, no. 4, pp. 442–456, 2005.
[57] Y Mo, "Production and marketing of nature rubber in 2009 and market forecast in 2010," *China Tropical Agric.*, vol. 33, no. 2, pp. 12–15, 2010.
[58] Statist. Bureau Hainan Province, Surv. Office Nat. Bureau Statist. Hainan, *Hainan Statistical Yearbook 2007*. Beijing, China: China Statist. Press, 2007.
[59] F. Deng, Q. Chen, and X. Chen, "Comparison of ecological service among nature forest, rubber and eucalyptus plantations," *J. South China Univ. Tropical Agric.*, vol. 13, no. 2, pp. 19–23, 2007.
[60] Statist. Bureau Hainan Province, Surv. Office Nat. Bureau Statist. Hainan, *Hainan Statistical Yearbook 1993*. Beijing, China: China Statist. Press, 1993.
[61] Ministry of Agriculture, P. R. China, "Technical regulations for cultivation of rubber tree," Beijing, China, 2006.

Bangqian Chen received the Master's degree in numerical material simulation from the Huazhong University of Science and Technology, Wuhan, China, and the Ph.D. degree in landscape ecology from Fudan University, Shanghai, China, in 2007 and 2017, respectively.

He is an Associate Researcher with the Rubber Research Institute, Chinese Academy of Tropical Agricultural and Sciences, Haikou, China. His main research interests include remote sensing of tropical forest and plantation, including map and monitor land cover and land use change of tropical forest, rubber plantation, and mangrove forest, and inversion of plantation parameters such as leaf area index and stand age, through integrating time series optical and SAR satellite imagery.

Xiangming Xiao received the B.Sc. degree in biology from Xiamen University, Xiamen, China, the Master's degree in plant ecology from the University of Science and Technology, Beijing China, and the Ph.D. degree in ecosystem science from Colorado State University, Fort Collins, CO, USA, in 1982, 1987, and 1994, respectively.

He is a Professor of ecology with the Department of Microbiology and Plant Biology, University of Oklahoma, Norman, OK, USA. He directs the Earth Observation and Modeling Facility (http://www.eomf.ou.edu), and is also an Associate Director with the Center for Spatial Analysis. He has been involved in interdisciplinary study in the areas of geospatial technologies, land cover and land use change, and terrestrial carbon cycle. He has studied agriculture, grassland, and forests in North America, Southern America, Africa, and Asia. He leads an effort in community remote sensing and manages a crowdsourcing and citizen science data portal, the Global Geo-Referenced Field Photo Library (http://www.eomf.ou.edu/photos/).

Huichun Ye received the Ph.D. degree in soil science from China Agricultural University, Beijing, China, in 2014.

He currently works with the Institute of Remote Sensing and Digital Earth, Chinese Academy of Sciences, Beijing, China. His current research interests include quantitative remote sensing application in vegetation monitoring and precision agriculture.

Jun Ma received the B.S. degree in environmental science from Hangzhou Normal University, Hangzhou, China, and the Ph.D. degree in ecology from the University of Chinese Academy of Sciences, Beijing, China, in 2010 and 2015 respectively.

He was working as a Postdoctoral Researcher with Fudan University, Shanghai, China, during 2015–2017. His study in post-doctor period was mainly focused on the succession and carbon sequestration dynamics of forest landscape using method of remote sensing and forest landscape models. He is currently working as an Associate Research Professor with Fudan University and studying the dynamics of vegetation productivity and biomass at regional scale.

Russell Doughty, photograph and biography not available at the time of publication.

Xiangping Li, photograph and biography not available at the time of publication.

Bin Zhao, photograph and biography not available at the time of publication.

Zhixiang Wu, photograph and biography not available at the time of publication.

Rui Sun, photograph and biography not available at the time of publication.

Jinwei Dong, photograph and biography not available at the time of publication.

Yuanwei Qin, photograph and biography not available at the time of publication.

Guishui Xie, photograph and biography not available at the time of publication.